Topography of valley networks on Mars from the Mars Express High Resolution Stereo Camera digital elevation models.

V. Ansan, N. Mangold, Ph., Masson, E. Gailhardis, G. Neukum

▶ **To cite this version:**

V. Ansan, N. Mangold, Ph., Masson, E. Gailhardis, G. Neukum. Topography of valley networks on Mars from the Mars Express High Resolution Stereo Camera digital elevation models.. Journal of Geophysical Research, 2008, 113, pp.E07006, doi:10.1029/2007JE002986. hal-00357166

HAL Id: hal-00357166
https://hal.science/hal-00357166

Submitted on 28 Apr 2021

HAL is a multi-disciplinary open access archive for the deposit and dissemination of scientific research documents, whether they are published or not. The documents may come from teaching and research institutions in France or abroad, or from public or private research centers.

L'archive ouverte pluridisciplinaire **HAL**, est destinée au dépôt et à la diffusion de documents scientifiques de niveau recherche, publiés ou non, émanant des établissements d'enseignement et de recherche français ou étrangers, des laboratoires publics ou privés.

Topography of valley networks on Mars from Mars Express High Resolution Stereo Camera digital elevation models

Véronique Ansan,[1] Nicolas Mangold,[1] Philippe Masson,[1] Evelyne Gailhardis,[1] and Gerhard Neukum[2]

Received 10 August 2007; revised 22 February 2008; accepted 17 March 2008; published 15 July 2008.

[1] Martian valley networks have been identified mainly in the Noachian heavily cratered uplands. The geometry of valley networks can be studied using Mars Orbiter Laser Altimeter (MOLA) altimetry, which is sufficient to map large valleys without a detailed 3-D shape of valley networks. Imaging from the Mars Express High Resolution Stereo Camera (HRSC) is used to generate digital elevation models (DEMs) with resolution $\leq$50 m and vertical accuracy <60 m. We studied valleys near Huygens crater and in the Aeolis region both in the Noachian bedrock and on the West Echus plateau in Hesperian bedrock. HRSC DEMs in these areas show that (1) drainage density is 3 times higher than is observed in MOLA data, (2) degree of ramification is 1 order more than with MOLA, (3) transverse valley profiles show a V shape more accurately and a minimum depth of $\sim$20 m, and (4) higher drainage density shows greater headward extension that is not correlated to greater valley depth. The deepest valleys (400 m) are found in the Huygens region, where the density in the DEM is 0.1 km^{-1}, compared to shallow valleys (<100 m) of the Echus region, where the density is higher ($\sim$0.3 km^{-1}). These regional differences are due to spatially variable preservation and bedrock lithology. Longitudinal profiles suggest variations in duration of activity: profile concavity is only developed in some Noachian terrains. Valleys visible in HRSC images correspond to topographic features in DEMs showing the same geometry as terrestrial valleys thought to be formed by overland flows and seepage.

Citation: Ansan, V., N. Mangold, P. Masson, E. Gailhardis, and G. Neukum (2008), Topography of valley networks on Mars from Mars Express High Resolution Stereo Camera digital elevation models, *J. Geophys. Res.*, *113*, E07006, doi:10.1029/2007JE002986.

1. Introduction

[2] Since the Mariner 9 mission of 1971–1972, widespread valley networks have been recognized in the heavily cratered terrain located in the southern hemisphere of Mars [*Schultz and Ingerson*, 1973; *Carr and Clow*, 1981; *Mars Channel Working Group*, 1983; *Carr*, 1996]. The valleys are arranged in a branching pattern similar to that of fluvial valley networks on Earth. For a few decades, different processes of their formation involving liquid water have been debated [*Milton*, 1973; *Sharp and Malin*, 1975; *Pieri*, 1980; *Baker and Partridge*, 1986; *Howard et al.*, 1988; *Squyres*, 1989; *Gulick and Baker*, 1989; *Baker*, 1990; *Baker et al.*, 1992; *Goldspiel et al.*, 1993; *Carr*, 1996; *Grant*, 2000; *Carr and Malin*, 2000; *Gulick*, 2001; *Howard et al.*, 2005; *Irwin et al.*, 2005b; *Mangold et al.*, 2004a, 2004b; *Ansan and Mangold*, 2006]. Because of their resemblance to the terrestrial fluvial valley networks, they have been interpreted as formed mainly by surface runoff [*Carr*, 1981; *Baker*, 1982, 1985; *Craddock and Howard*, 2002; *Mangold et al.*, 2004a, 2004b; *Howard et al.*, 2005; *Irwin et al.*, 2005b; *Ansan and Mangold*, 2006]. However, surface runoff is often rejected because of the low drainage density and the low degree of valley organization [e.g., *Carr and Chuang*, 1997; *Cabrol and Grin*, 2001; *Stepinski and Collier*, 2003]. Alternatively, it has been suggested that groundwater sapping triggered by geothermal or hydrothermal heating was predominant [*Sharp and Malin*, 1975; *Pieri*, 1980; *Howard et al.*, 1988; *Tanaka et al.*, 1998; *Malin and Carr*, 1999; *Dohm and Tanaka*, 1999; *Gulick and Baker*, 1990; *Gulick*, 1998; *Goldspiel and Squyres*, 2000], which is supported in relatively few places by the regional volcanic and tectonic context. After the Mariner 9 and Viking missions, many authors concluded that groundwater sapping formed the Martian valley networks, but new discoveries from the Mars Global Surveyor [*Albee et al.*, 1998], Mars Odyssey [*Christensen et al.*, 2003] and Mars Express [*Chicarro et al.*, 2004] missions have led to a shift to a runoff or combined runoff/groundwater sapping origin [e.g., *Craddock and Howard*, 2002; *Mangold et al.* 2004a; *Howard et al.*, 2005; *Irwin et al.*, 2005b; *Ansan and Mangold*, 2006].

[3] As valley networks incised the Noachian (>3.7 Ga) heavily cratered terrain [*Tanaka*, 1986; *Hartmann and Neukum*, 2001; *Hartmann*, 2005], they probably formed at

[1]Laboratoire IDES-UMR 8148 CNRS, Université Paris-Sud, Orsay, France.
[2]Institute of Geosciences, Freie Universität Berlin, Berlin, Germany.

Copyright 2008 by the American Geophysical Union.
0148-0227/08/2007JE002986

the end of the Noachian Period or just at the beginning of the Hesperian. However, several dendritic, fluvial valley networks have been detected using Thermal Emission Imaging System (THEMIS) infrared images [*Christensen et al.*, 2003] on the plateau of West Echus Chasma [*Mangold et al.*, 2004a, 2004b] at the eastern side of the Tharsis region. These valley networks incised volcanic plateau material that covered the region during the Hesperian Period (3.7–3.0 Ga), based on relative chronology and crater counts [*Tanaka*, 1986; *Mangold et al.*, 2004a]. This finding suggests that liquid water was still present at the surface, at least episodically, during the Hesperian Period.

[4] Most studies have used two dimensional data sets at horizontal scales ranging from 1 km to few meters [*Carr*, 1981; *Baker*, 1985; *Malin and Edgett*, 2000; *Mangold et al.*, 2004a; *Ansan and Mangold*, 2006], including both visible images (Viking, visible THEMIS and Mars Orbiter Camera (MOC) [*Malin et al.*, 1998]), and THEMIS infrared images. Using the altimetry acquired by the Mars Orbiter Laser Altimeter (MOLA) [*Smith et al.*, 1999], the geometry of valleys has been studied at spatial scale of ~500 m with a vertical accuracy of 1 m. The main valleys often have a width of a few kilometers and a depth of ~100 m [*Williams and Phillips*, 2001]. Valley networks identified by an automated program using MOLA data have a low degree of organization associated with a low drainage density [*Stepinski and Collier*, 2003; *Stepinski and Stepinski*, 2005; *Ansan and Mangold*, 2006]. The MOLA spatial resolution is sufficient to map the main valleys, but not their small tributaries that are visible on the high-resolution imagery.

[5] Since January 2004, the High Resolution Stereo Camera (HRSC) on board the European Mars Express orbiter has acquired along its orbital ground tracks a set of stereo panchromatic images with a spatial resolution of a few tens of meters per pixel [*Wewel et al.*, 2000; *Neukum et al.*, 2004; *Jaumann et al.*, 2007]. From each triplet of HRSC images, it is possible to generate a digital elevation model (DEM) with improved spatial resolution $\leq$50 m pixel^{-1}, superior to that of MOLA. In contrast, the vertical accuracy is not as good as that of MOLA, ranging up to a few tens of meters depending on terrain roughness and image quality [e.g., *Jaumann et al.*, 2007]. The HRSC DEM can be used to better constrain the geometry of valleys and determine which process(es) were responsible for their formation.

[6] Three Martian regions are studied here: (1) the Noachian terrain of Terra Cimmeria (South of Aeolis region), (2) a Noachian region east of the Huygens impact crater (NW of the Hellas basin), and (3) the Hesperian terrain of the West Echus Chasma plateau. For each region, we first present the manual mapping of valley networks performed from HRSC visible images. We then automatically extract valley networks from the two topographic data sets (MOLA and HRSC DEMs) and we compare the geometry of valleys mapped in the three data sets.

2. Methodology

2.1. MOLA Altimetry

[7] The altimetry measured by MOLA during the Mars Global Surveyor mission allows us to study the geometry of valleys at a spatial resolution of ~500 m with a height accuracy of ~1 m [*Smith*, 1998; *Smith et al.*, 1999]. For the studied regions, MOLA altimetry was projected onto the Martian ellipsoid with an equatorial axis of 3396.19 km and a polar axis of 3376.20 km, defined by the International Astronomical Union as the Mars IAU 2000 [*Seidelmann et al.*, 2002], with a sinusoidal projection centered at a given meridian. The geographic coordinates follow the Martian standard coordinate system with planetocentric latitudes and east longitudes [*Duxbury et al.*, 2002]. The MOLA altimetry and other data sets are then included in geographic information systems (ArcView and Er-Mapper).

2.2. HRSC Images

[8] The HRSC camera acquired images in five panchromatic channels under different observation angles, as well as four color channels at relatively high spatial resolution [*Neukum et al.*, 2004]. In our work we used only the panchromatic nadir image, in which the spatial resolution reaches generally ~10 to 50 m pixel^{-1}, and the two panchromatic stereoscopic images with a spatial resolution of similar range to four times lower than that of the nadir image (Figure 1a).

[9] The first step of HRSC image processing is their ortho-rectification, producing level 2 images (Figure 1b). Using the photogrammetric software developed both at the Deutsches Zentrum für Luft- and Raumfahrt (DLR) and the Technical University of Berlin [*Scholten et al.*, 2005], we projected level 2 images onto a reference surface corresponding to the MOLA topography with a spatial grid of 5 km pixel^{-1} [*Smith et al.*, 1999; *Neuman et al.*, 2003], a sinusoidal projection at a given central meridian, and the best spatial resolution, taking into account the spacecraft position, the camera orientation along the ground track and the camera characteristics included in exterior orientation data (Figure 1b). The coordinates of ortho-rectified nadir images are defined in the planetocentric system of the Mars IAU 2000 ellipsoid [*Seidelmann et al.*, 2002, *Duxbury et al.*, 2002].

2.3. HRSC Digital Elevation Model

[10] Here we describe the different steps to generate the HRSC DEMs using the photogrammetric software developed at the DLR and the Technical University of Berlin [*Scholten et al.*, 2005; *Albertz et al.*, 2005; *Gwinner et al.*, 2007]. The first step includes the rectification of nadir and stereo images at the same scale (geometric image correction and map projection). The second step consists of the image correlation in order to find the location of homologous points in the different HRSC images, using a matching process at a different spatial grid size [*Scholten et al.*, 2005] (Figure 1c). The third step is the calculation of the spatial location of 3-D object points, defined by Cartesian coordinates in a fixed-body Martian reference system, using forward ray intersection defined by homologous points and available orientation data (stereo model) (Figure 1d). The location of each 3-D object point is defined with its accuracy in three dimensions (σx, σy, and σz) [*Scholten et al.*, 2005; *Albertz et al.*, 2005]. At this step, we remove all 3-D object points that are imprecisely located, e.g., σx, σy and σz must be <100 m. The fourth step is the transformation of Cartesian coordinates of 3-D object points in geographic latitude, longitude, and height projected on the

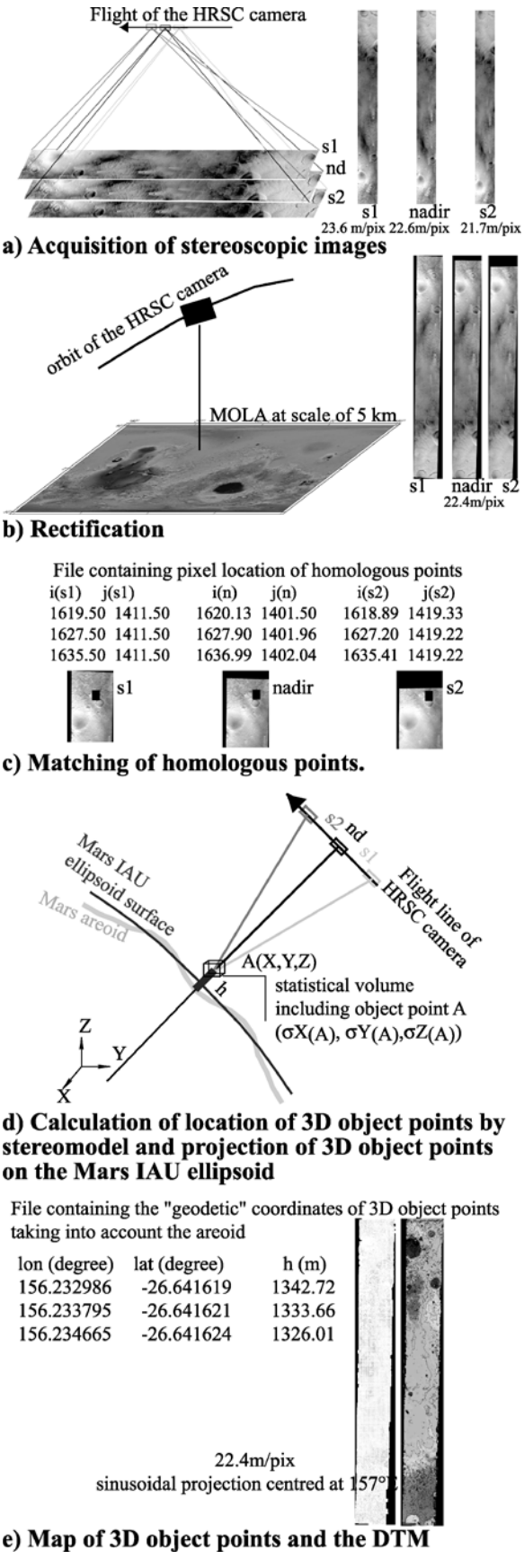

MARS IAU ellipsoid [*Duxbury et al.*, 2002; *Seidelmann et al.*, 2002] (Figure 1d). The height is calculated taking into account the Martian geoid defined as the topographic reference for the Martian heights, i.e., the areoid [*Smith*, 1999]. The last step consists of the generation of two maps at the same scale of rectified images using VICAR image processing system (Multisession Image Processing Laboratory, The VICAR Image Processing System, 2005): one map of the locations of 3-D object points, and one DEM in which the gap areas are filled by height interpolation (Figure 1e).

[11] The choice of the DEM's cell size is influenced by the spatial distribution of 3-D object points bounding the geological features. Given the heterogeneous distribution of these points in the DEM and the desire to accurately characterize the geologic features, we choose the smallest grid cell size that leaves >70% of the cells filled. We take caution not to extract topographic information in areas devoid of points. The resolution of the resulting DEM is thus often two to three times larger than that of the original image resolution. The calculated height accuracy is usually $\sim$20 m when geometric parameters of the HRSC camera, the terrain roughness, and the image quality are optimal. Nevertheless, a height offset relative to the MOLA reference exists and is usually <50 m, locally reaching 100 m.

2.4. Extraction of Valley Networks

[12] We manually mapped valley networks from the nadir images at 10 to 50 m pixel^{-1}, taking into account the geological features (impact craters, faults, landslides, etc) that have modified the geometry of valleys after their formation. We used a hydrologic analysis system, DNR hydromod, included in ArcView GIS [*Loesch*, 2001], to extract valley networks from the DEMs. The automatic detection is mainly used to provide a comparison point between each data set, not to use the method as an independent mapping system of valleys on Mars. The automatic detection of valleys in DEMs always requires a visual control to verify the presence of valleys in the images.

[13] The DNR hydromod program consists of three steps of processing: (1) the original topography (DEM) is modified, removing sinks to produce a continuous flow direction grid. This step is very important because sinks like pits or impact craters disrupt the drainage topography; (2) a flow direction grid is calculated where the steepest downslope direction is recognized from each cell to the eight neighboring cells (D8 algorithm); and (3) a flow accumulation

Figure 1. Different steps of DLR's photogrammetric software program for generating the HRSC digital elevation models (DEMs). (a) Acquisition of the triplet of the HRSC images (s1, stereo image 1; nd, nadir image; and s2, stereo image 2). (b) Image rectification using the camera properties, the geometry of acquisition, and the MOLA DEM at 5 km resolution. (c) Matching to find the homologous points in the triplet of images. The pixel location (i, j) is recorded in a file. (d) Calculation of the Cartesian location of 3-D object points and the determination of height above the areoid. (e) Map containing the location of 3-D object points and the DEM obtained after interpolation.

grid is generated as the cumulative number of cells flowing into each downslope cell. Cells that have high accumulation of flow may be used to identify stream channels. This software therefore permits one to deduce the probable location of river (stream flow) based on the topography.

[14] Rivers do not exist on Mars at present, but the location of old streams deduced from DNR Hydromod could correspond to the locations of past river channels. In few cases, channels have been identified on the Martian surface and are interpreted as the imprint of old rivers [e.g., *Carr and Malin*, 2000; *Irwin et al.*, 2005a*; Jaumann et al.*, 2005]. In our study, no channel has been identified, and we assume that stream flows detected in topography correspond to old rivers flowing downstream inside valleys. Valleys that are not visible in the HRSC images (e.g., in flat areas, in closed depressions with flat interiors, and in small impact craters) were deleted in the automatic mapping. Only the lengths of individual valley network segments and the remaining area containing valley networks were used to calculate drainage densities.

[15] As the detection of stream channels depends on the flow accumulation, the comparison of the organization of valley networks from two DEMs at different spatial scales is mainly controlled by the threshold on the cumulative number of cells flowing into each downslope one that defines a valley head. For this reason, we determined the minimum cumulative number of cells flowing into a downslope cell for which the stream channels are detected in the MOLA DEM. Then, we applied this threshold multiplied by the scale ratio between the MOLA and the HRSC DEMs for detecting stream channels in the HRSC DEM. For example, a minimum of 900 cells of accumulation flow for a MOLA DEM at 450 m pixel^{-1} compares to a minimum of 18,000 cells for a HRSC DEM at 22.4 m pixel^{-1}.

2.5. Morphometric Parameters Used for Valley Networks Characterization

[16] Drainage basins are defined as the area in which liquid water and sediments are collected and transported, bounded by the highest topographic points. We compared among the different data sets the location of detected valleys, their number, and their magnitude in *Strahler*'s [1952] system. In this system, each valley segment is assigned to an order: the first order is a segment with no tributary. Where two segments of first order join together, they form a second-order segment, and so on. Where two segments of different orders join together, the next segment retains the higher order of the upstream segments. The highest order of a valley network corresponds to that of the longest tributary called the main tributary. The linear relationships between valley order and the number of segments with a given order, and their length have been firmly established for well-developed networks [*Schumm*, 1956]. The bifurcation ratio (Rb) is the ratio of the number of valleys of a given order (N_u) to the number of valleys in the next higher order (N_{u+1}). The length ratio (Rl) is the ratio between the average length of valleys of a given order (L_u) to that of the next higher order (L_{u+1}) [*Horton*, 1945; *Strahler*, 1952]. We also determined the drainage density (km^{-1}) of different drainage basins, i.e., the sum of the length (km) of all individual valleys divided by the drainage basin area (km^2).

[17] The analysis of individual valley topography allows us to determine the stage of erosion. The valley longitudinal profile is defined as the thalweg changes in elevation down valley. It corresponds to the river incision in response to variations in climatic and tectonic effects, as well as local changes in hydraulic parameters (water discharge and load) and lithology. We compared the shape of longitudinal profiles extracted from the MOLA and HRSC DEMs for different valley networks. The transverse profiles were extracted at different locations in the downstream direction, in order to see the variations in shape from the head to the mouth of major tributaries. For example, the transverse profile can show a transition from an upstream V shape to a more rectangular/trapezoidal shape downstream that can be due to alluvial infilling.

3. Results Over Three Martian Regions

[18] We present below, for each studied region, (1) the morphometric analysis at the regional scale showing the results of manual mapping on the nadir image, the results of the DEM calculation, and the automatic detection of valleys, respectively, and (2) the detailed analysis of some drainage basins with their longitudinal and transverse profiles. These different regions have been imaged by the HRSC camera during different geometries of acquisition (e.g., different orbital parameters including date and hour of acquisition, and the height of the camera along an elliptical orbit), which highly influence the spatial resolution of nadir and stereo images. We discuss the impact of these parameters on the quality of the HRSC DEMs and the limit of valleys detection in the HRSC DEM compared to that with the MOLA data.

3.1. Valley Networks in the South Aeolis-Terra Cimmeria Region

[19] We studied the valley networks that incised the Terra Cimmeria within the Aeolis and Eridania quadrangles. These valleys have previously been studied using Viking images [*De Hon*, 1978; *Scott and Carr*, 1978; *Scott et al.*, 1978, 1986, *Brakenridge*, 1990, *Greeley and Guest*, 1987]. Terra Cimmeria consists essentially of Noachian terrains (>3.7 Ga) including geologic units mapped as the old heavy cratered plateaus (Npl1), local subdued cratered terrain (Npl2) interpreted as the result of the early stage of widespread volcanism or mantling, and dissected highlands (Npld) cut by valley networks [*Scott et al.*, 1986]. Small intercrater plains (Hr) are interpreted as extensive lava flows formed during the Early Hesperian Epochs [*Scott et al.*, 1986]. These plains are topographically smooth except that they are crossed by wrinkle ridges. The latter are likely due to compressional tectonism that locally extends into the heavily cratered plateau [*Watters*, 1993].

3.1.1. Morphometric Analysis at the Regional Scale

3.1.1.1. HRSC Image Analysis

[20] The HRSC camera acquired two sets of images during the H0228 and H0241 orbits. They are located at the boundary of the Aeolis and Eridania regions between 156 and 158°E and 26°–36°S (Figure 2). Thanks to the low altitude of Mars Express orbiter (~266 km), all panchromatic images have a good spatial resolution of 21.7 m pixel^{-1} for the nadir image, 22.6 m pixel^{-1} for the stereo1

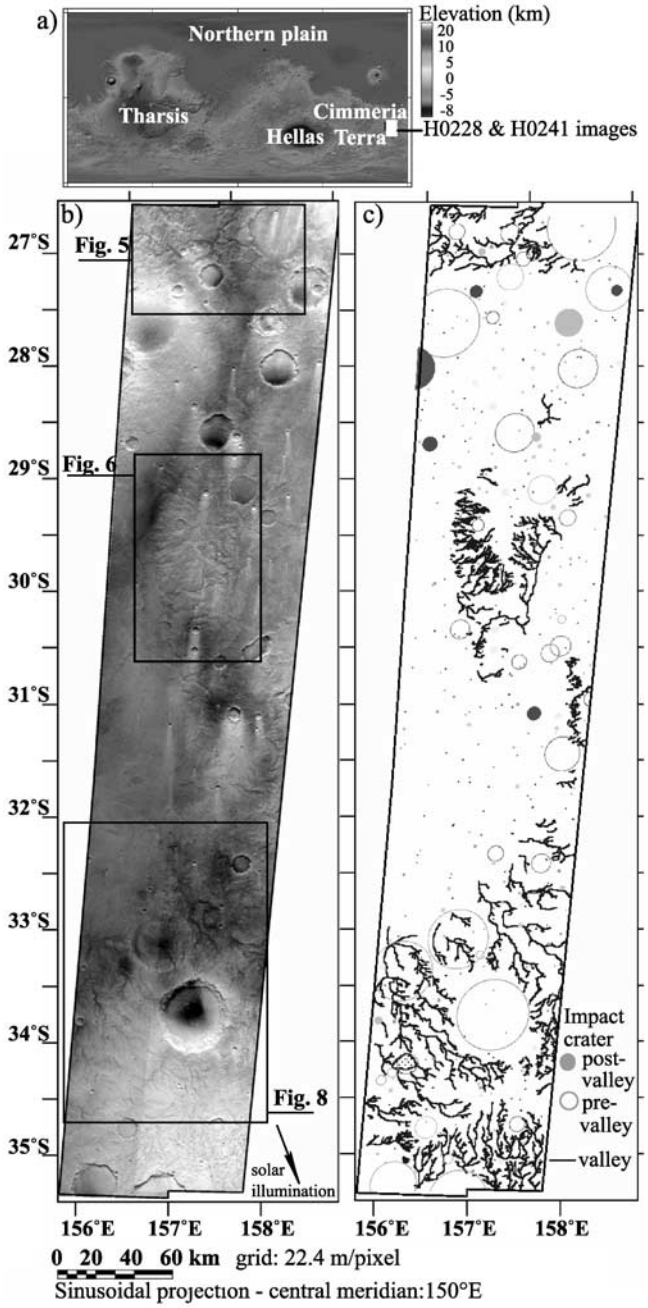

Figure 2. The southern part of the Aeolis region observed by two triplets of the HRSC images (H0241 and H0228). (a) Location of HRSC images on the MOLA map, eastward of the Hellas basin in Terra Cimmeria. (b) Mosaic of the HRSC H0241-H0228 nadir images at 22.4 m pixel^{-1}. Solar illumination comes from the NW. The three inner boxes correspond to the locations of Figures 5, 6, and 8. (c) Map of valley networks incising cratered highlands performed manually by classic photointerpretation methods.

image and 23.6 m pixel^{-1} for the stereo2 image, corresponding to the pixel size at the center of images for the H0228 and H0241 orbits. These two nadir images have been projected in sinusoidal projection centered at longitude 150°E with a spatial grid size of 22.4 m pixel^{-1} and mosaicked in order to cover the whole region (Figure 2).

[21] Numerous valley networks incised Noachian rough, heavily cratered regions (Figure 2). Valleys crosscut old degraded impact craters in the southern part of the mosaic. In contrast, the western part of the mosaic of nadir images lacks valleys and presents few impact craters, suggesting that the area would be an intercrater plain (Hr) as defined by *Scott et al.* [1986]. Valley networks and impact craters have been mapped through the whole HRSC mosaic (Figure 2). Valley networks seem to reach a broad extension because a large number of tributaries valleys have dissected the drainage basins reaching a Strahler order of five for the most developed ones, specifically a valley network located at 33.0°S–157.5°E [*Masson et al.*, 2005; *Ansan et al.*, 2005, 2007a, 2007b].

3.1.1.2. Calculation of the HRSC DEM

[22] To generate the HRSC DEM, we ortho-rectified the nadir and stereo images with the exterior orientation data at the same scale of 22.4 m pixel^{-1}. We found 17,726,308 homologous points (Figure 3c) for which 3-D coordinates have a good spatial accuracy (σx = 14.5 m, σy = 5.6 m and σz = 9.4 m). The statistical height error is 13 m on each point. The number of 3-D object points being relatively high, we generated a DEM with a spatial grid equal to the original images (22.4 m pixel^{-1}) in sinusoidal projection centered on the 150°E meridian. The spatial distribution of 3-D object points is quite homogeneous, and only 21.9% of the total area is empty (Figure 3c). These gaps are not problematic for valley geometry, because most of them occur in smooth plains or crater floors, therefore out of the locations with abundant valleys. We generated the DEM by interpolation (Figure 3b). Taking MOLA as a reference, we calculated the height offset between the HRSC DEM and MOLA. The mean regional height offset is relatively low (<25 m), but it becomes larger on the inner rim of large impact craters, reaching more than 100 m in a few places (Figure 3d). At the regional scale, the HRSC DEM shows the same topography as MOLA: a plain in the western part standing at an elevation of 800 m, bounding a cratered highland rising up to 2200 m in the SE corner of the DEM.

3.1.1.3. Automatic Extraction of Valley Networks

[23] The extraction from MOLA data was done with a minimum threshold of 900 cells of accumulation flow at the MOLA DEM scale of 450 m (Figure 4). A total of 24 drainage basins (Table 1) located in the cratered highlands have been detected, generally covering small areas (average ~545 km^2), except that three basins (J, N, P) exceed 1000 km^2 (Table S1 in the auxiliary material).[1] Basins are relatively elongated and parallel to the slope. They are incised by a few (<10) tributaries that correspond to the main ones observed on HRSC images. The drainage density calculated using MOLA ranges from 0.01 to 0.17 km^{-1} with a maximum Strahler order of 3. For example, the widespread drainage basin N, located at 33.0°S–157.5°E, covers 4089.70 km^2. It contains 7 tributaries incising 215.81 km in totality, which organize with a Strahler order of 2. Its drainage density is 0.05 km^{-1} close to the regional average one.

[24] In comparison, 60 drainage basins have been detected automatically in the HRSC DEM with a minimum

[1] Auxiliary materials are available in the HTML. doi:10.1029/2007JE002986.

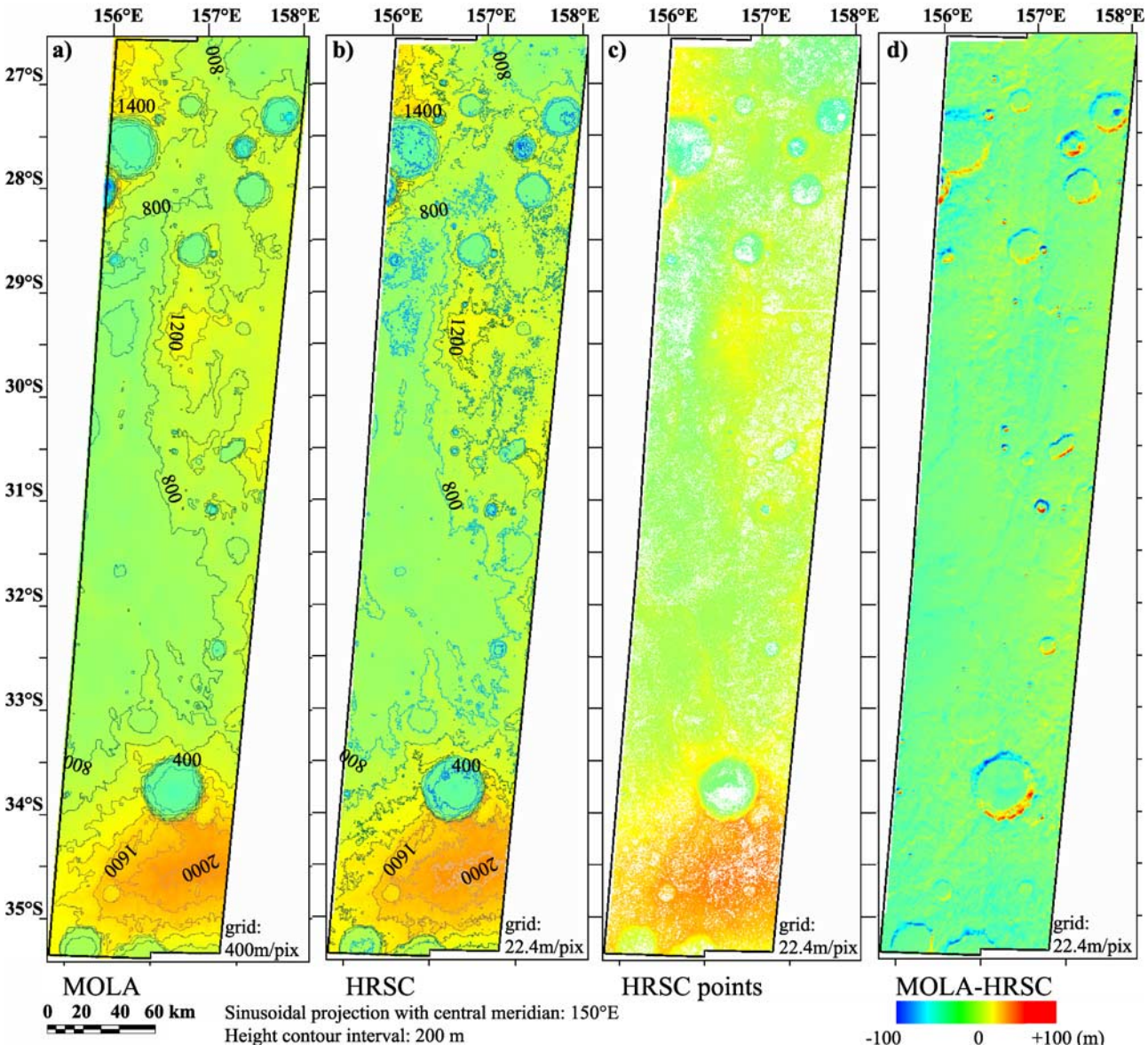

Figure 3. (a) The MOLA topographic map of this area at 400 m pixel^{-1}. (b) HRSC DEM generated from the population of 3-D object points. (c) Distribution of 3-D object points in a regular grid of 22.4 m pixel^{-1}. (d) Vertical offset between MOLA and the HRSC DEM. All maps are in sinusoidal projection centered at 150°E longitude. Height contour interval is 200 m.

threshold of 18,000 cells of accumulation flow (Figure 4). Notice that the high number of cells is due to the grid sampling ratio: the 900 cells for the 450 m pixel^{-1} MOLA grid compare to 18,000 cells at the 22.4 m pixel^{-1} resolution of HRSC DEM. In the latter data set, basins have a mean area of 122 km^2 (Table 1 and Table S2). Basins J, N and P remain the same size as in the MOLA DEM. The shape of the basin remains elongated and oriented down the regional slope. The number of tributaries increases significantly in each basin (>10), and the drainage density ranges from 0.09 to 0.45 km^{-1} with a maximum Strahler order of 4. The drainage basin N in the HRSC DEM covers a slightly smaller area than in MOLA, i.e., 2257.16 km^2, due to a better topographic grid resolution. The drainage basin N contains 49 tributaries totaling 425.46 km and organized with a Strahler order one point higher than in MOLA (fourth order). Its drainage density of 0.19 km^{-1} calculated from the HRSC DEM is therefore a factor of 3.8 greater than in MOLA.

[25] We compared these automatic extractions to the manual mapping. For example, the drainage basin N is defined by the highest points surrounding the drainage area in the HRSC DEM. The manual mapping shows that the divide of this basin fits very well with its limit observed on the HRSC image. The drainage basin N is incised by 148 tributaries with a network Strahler order of 5, i.e., the highest Strahler order found in this studied area. The total length of tributaries is 626.67 km, giving a drainage density

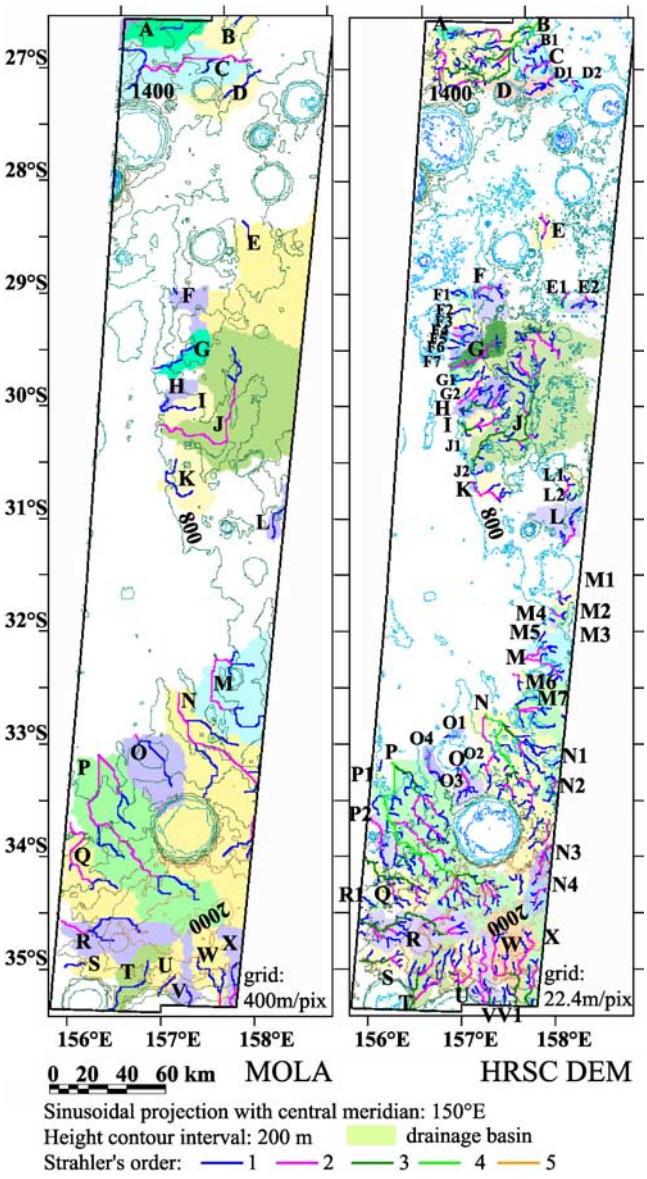

Figure 4. Comparative maps of valley networks detected automatically in MOLA and the HRSC DEM with different spatial resolution. Drainage basins are bounded by their colored area and each is assigned a letter. Each Strahler order is identified by a color.

of 0.28 km^{-1}, 1.5 times higher than that found in HRSC DEM. The highest drainage density is found in the drainage basin P (0.54 km^{-1}), which is only fourth order.

[26] In summary, we observe that the drainage density increased from the MOLA data to the HRSC DEM by a factor >3, but it is still slightly lower than was found in the manual mapping. The HRSC DEM therefore gives a strong improvement in the characterization of drainage basins compared to MOLA. In addition, the tributaries automatically extracted from the HRSC DEM correspond to the major tributaries observed on the HRSC image, which validates the quality of DEM related to the "ground truth" of the image.

3.1.2. Detailed Analysis of Drainage Basins

[27] The HRSC images (Figure 2) display three patterns of valley networks distributed in the north (Figure 5), the center (Figures 6 and 7), and the southern parts (Figures 8, 9, and 10) of Terra Cimmeria study area.

3.1.2.1. Northern Part

[28] In the northern part of the studied region (Figure 5), highlands stand at 800 m above the surrounding plain with a regional slope to the NE (Figure 3). The HRSC images display a cratered terrain in which most large impact craters (>10 km in diameter) have a flat floor and degraded rim, whereas most smaller impact craters have a typical bowl shape (Figure 5). These highlands have been carved by numerous valley networks that also crosscut rimless impact craters, such as those present in the NE corner of Figure 5. The valley networks have few visible tributaries but display a branching pattern. The valleys have a dark-toned, flat floor without exposed inner channels, suggesting that the floors may have been mantled by sand and dust after the time of valley incision [*Carr and Malin*, 2000; *Wilson and Zimbelman*, 2004; *Ansan and Mangold*, 2006], although no dune is observed in this area at the HRSC scale.

[29] The path of the main tributary (Bup to Bdw) follows the regional slope (Figure 5b). In the downstream direction it is deviated to the North (Figure 5b). A second valley network develops on the eastward slope converging into the large rimless impact crater to the east. The two valley networks are very close to each other (near cross section EF in Figure 5b), suggesting that an impending capture did not occur because of the cessation of erosion. When we superimpose the valley networks detected automatically in the HRSC DEM to the image viewed in 3-D (Figure 5c), we observe that valleys follow the current topography.

[30] Transverse profiles along the main tributary (Figure 5d) show that gridded MOLA data generally underestimate the depth of valleys and show a lower accuracy in width. Whereas the MOLA transverse profiles indicate 3-km width, 100-m depth, and an open V shape, the HRSC transverse profiles are more accurate with <1-km-wide and ~100-m-deep valleys that have steeper sides. Moreover, the HRSC DEM allows us to detect several valleys where MOLA detected just one at their confluence (Figure 5d, cross section EF). Using the HRSC DEM, we observe a downstream increase in the width of the main tributary from 1 km to 2 km, associated with an increase in depth of 50 m to 100 m.

[31] The longitudinal profiles of the main tributary are similar with MOLA and the HRSC DEM. We see that the mean height offset is low (<25 m) along the longitudinal profile (Figure 5e), which is relatively accurate. The profile is not smooth with high-frequency variations in height at the scale of <50 m. The height frequency can be locally due to the calculation method of the HRSC DEM, given the calculated average height accuracy of 13 m, but the fact that we see similar effect on MOLA data argues against a problem of the HRSC DEM only. Most of the heterogeneity along topographic profiles is likely due to a later evolution such as superposed impact craters, crater ejecta, small landslides, etc., that have degraded the original shape of the valley floor. Using the HRSC DEM, we measured a regional regular slope of 0.4°, with a rather linear slope close to the regional terrain slope.

Table 1. Morphometric Parameters of Different Studied Regions

	Aeolis			Huygens			Echus Plateau		
	MOLA 400 m pixel^{-1}	HRSC DEM 22.4 m pixel^{-1}	HRSC Image 22.4 m pixel^{-1}	MOLA 450 m pixel^{-1}	HRSC DEM 250 m pixel^{-1}	HRSC Image 50 m pixel^{-1}	MOLA 450 m pixel^{-1}	HRSC DEM 50 m pixel^{-1}	HRSC Image 20 m pixel^{-1}
Number of basins	24	60	60[a]	97	129	129*	17	45	45*
Mean surface of basin (km^2)	545 ± 250	122 ± 100	122 ± 100	180 ± 150	160 ± 150	160 ± 150	392 ± 200	71 ± 47	71 ± 47
Mean total length of tributaries (km)	36 ± 10	28 ± 10	34 ± 11	19 ± 7	17 ± 8	36 ± 17	32 ± 8	11 ± 3	25 ± 6
Mean drainage density (km^{-1})	0.06 ± 0.03	0.23 ± 0.07	0.27 ± 0.11	0.10 ± 0.04	0.11 ± 0.05	0.22 ± 0.11	0.08 ± 0.04	0.15 ± 0.06	0.35 ± 0.12
Maximum of drainage density (km^{-1})	0.17	0.45	0.54	0.22	0.23	0.29	0.15	0.30	0.80
Maximum Strahler order	3	4	5	3	4	4	3	4	5
Number of basins with Strahler order at least 3	2	19	43	8	14	60	2	7	7
Mean drainage density (km^{-1})	0.04 ± 0.03	0.22 ± 0.06	0.22 ± 0.11	0.11 ± 0.03	0.13 ± 0.04	0.12 ± 0.04	0.09 ± 0.01	0.18 ± 0.04	0.50 ± 0.20
Mean bifurcation ratio (Rb)	2.5 ± 0.3	3.4 ± 1.0	-	3.0 ± 0.8	3.3 ± 0.7	-	2.9 ± 0.5	2.9 ± 0.9	-
Mean length ratio (Rl)	1.0 ± 0.1	2.1 ± 1.2	-	1.8 ± 1.2	2.0 ± 0.8	-	1.9 ± 0.6	1.6 ± 0.6	-

[a]The number of basins is the same as that in the HRSC DEM because we use the topographic definition of a drainage basin.

3.1.2.2. Central Part

[32] In the central part of the south Aeolis images (Figure 6), an elongated highland stands at 1200 m with a relief of 400 m above the western intercrater plain (Figure 6). This highland has a few rimless impact craters that are crosscut by valleys, but fresh bowl-shaped impact craters are superposed on valley networks (Figure 6a). Numerous valley networks incised the western side of the upland where the slope is regular (1.5°). Valleys are narrower and more parallel than in the previous example, which is likely due to the regional slope (valleys tend to be subparallel on slopes above 1.5° [*Schumm*, 1956]). They vanish at the boundary of the smooth plain. The eastern side of the highland is less dissected by valley networks, but a long tributary (J) winds across the highland to reach the western plain (Figure 6b). Valleys follow the current regional slope, which is evident when we superpose the valley networks detected automatically in the HRSC DEM on an image viewed in 3-D (Figure 6c).

[33] Transverse profiles were plotted along the main tributary J (Figure 7). The HRSC profiles have many more details than do their MOLA equivalents. The HRSC DEM allows us to extract narrow (<250 m) and shallow (<25 m) valleys not detected at the MOLA scale. Moreover, we observe that the location of the thalweg in both data sets often shows a lateral offset up to 500 m, which is partially due to the low spatial resolution of MOLA. Using the HRSC DEM, we observe that the main tributary J increases in width increases downstream, from 250 m up to 2.5 km, and its depth increases as well from 30 m to 100 m.

[34] The HRSC longitudinal profile J is quite close to the MOLA-derived profile with a mean height offset of <20 m (Figure 7). The longitudinal profile has a concave shape in the upstream reach. The downstream reach displays a slightly convex shape that could indicate either that the rocks are more resistant to erosion or that a late, subtle topographic change occurred, preventing the stream from reaching a hydraulic equilibrium.

3.1.2.3. Southern Part

[35] The southern part of the south Aeolis image (Figure 8) is spectacular, with a large number of valleys that incised the highlands up to 2200 m in elevation (Figure 8). These highlands have many large (>20 km in diameter), flat-floored impact craters with degraded rim but without visible ejecta, e.g., the impact crater Odw in Figure 8b. Some of the craters are rimless, e.g., the impact crater in the NE corner of Figure 8. The NW part of the area contains a poorly cratered, smooth plain that is modified by N-S trending wrinkle ridges and stands at 800 m elevation. The 1400 m of relief has been incised by valleys which the highest heads are located just 300 m below the highest topographic point in the SE corner. Valley networks diverged in a radial pattern around the highest topographic point (Figure 8), and some of them (tributaries Pup-Pdw, Oup-Odw and Ndw-Nup) reached the NW plain in which they vanished. The main tributary O crosscuts an old flat-floored, impact crater with a degraded rim.

[36] In Figure 9a, a MOLA profile displays one 4-km-wide and 75-m-deep valley, whereas the HRSC profile shows two 1-km-wide and 100-m-deep valleys. Near the outlets of valleys P, O and N (Figure 8), the valley width is ~2 km and the depth is ~100 m (Figure 9b). The shallower valley detected by the HRSC data has a depth of 25 m near the head (Figures 9c and 9d). The different HRSC transverse profiles across the valley networks show that the main tributaries increase in width downstream.

[37] The longitudinal topographic profiles of these three main tributaries (Figure 10) display the same shape in both topographic data sets without significant offset (<50 m). However, they are quite different from each other. The 100-km-long longitudinal profile N displays a concave shape with its head incising the rim of the central 30 km-in-diameter impact crater. The stream eroded a sloping plain that drops 700 m with a regional slope of 0.4°. Even omitting the local 100-m-high, later wrinkle ridge (Figure 10), the slope of the longitudinal profile of this tributary N differs from the regional slope. The longitudinal profile O is somewhat shorter than the others: it follows the local topography and the border of the highly degraded rim of impact crater O (Figures 8 and 10). The 150-km-long longitudinal profile P begins at the top of the highland (2040 m) and follows the regional slope (0.5°)

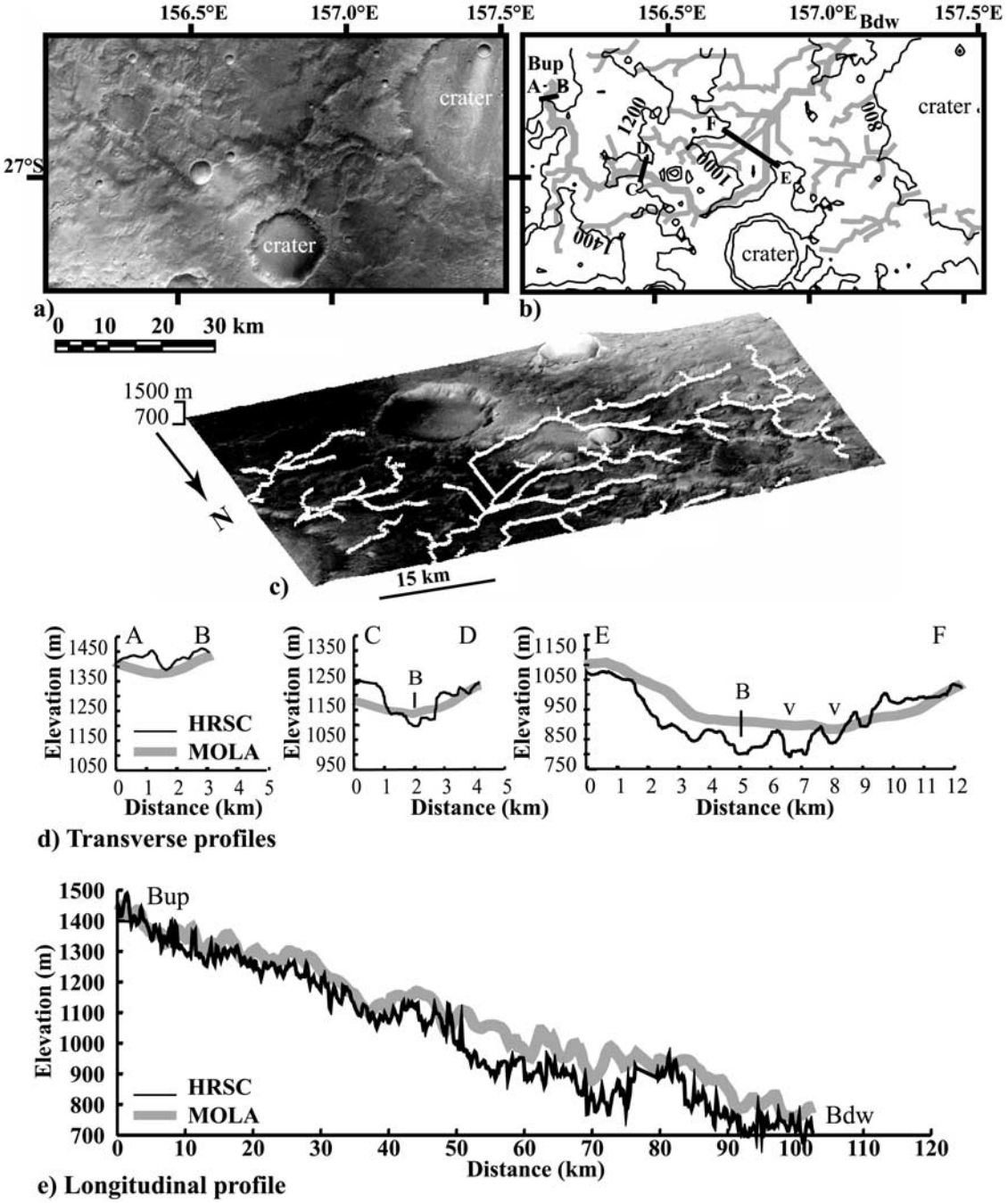

Figure 5. Detailed study of the northern part of the south Aeolis region (Figure 2). (a) Detail of the H0228 and H0241 nadir images (22.4 m pixel^{-1}). (b) Locations of valley networks (gray lines) detected automatically in the HRSC DEM. The widest (Bup-Bdw) corresponds to the main tributary of drainage basin B. Thick black lines labeled AB, CD, and EF correspond to the locations of transverse topographic profiles (Figure 5d). The contour interval (thin black lines) is 200 m. (c) A 3-D view of the HRSC image superimposed on the HRSC DEM showing a low topographic slope toward the NE. The valley networks detected automatically in the HRSC DEM are overlaid on the 3-D view. (d) Transverse profiles across the main tributary. Notice that the HRSC profile EF shows three valleys (v) in place of the major tributary B, contrary to that observed on MOLA profile. (e) Longitudinal profile along the main tributary (Bup-Bdw) showing a slightly concave shape.

before reaching the smooth plain 1300 m lower. Omitting the late wrinkle ridge that crosscuts the main tributary P, the longitudinal profile has a slightly concave shape.

[38] In summary, the valley networks in the south Aeolis-Terra Cimmeria region show dendritic to subparallel patterns according to the regional topographic slope, increasing width in the downstream direction, and different elevations

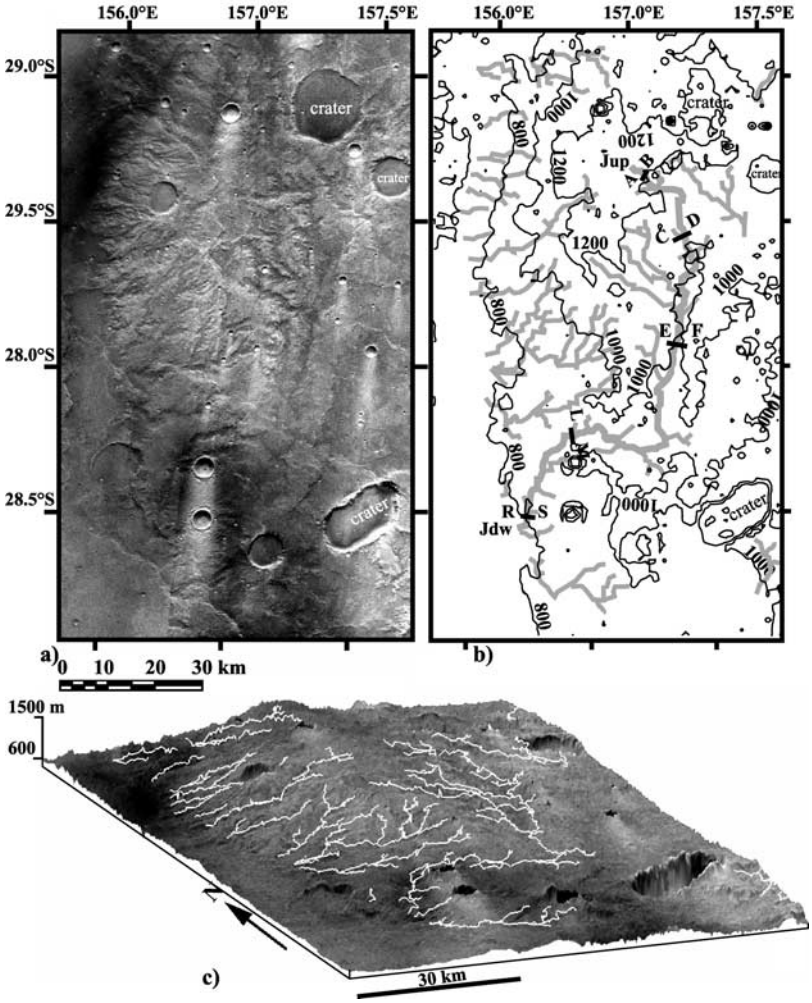

Figure 6. Detailed study of the central part of the south Aeolis region (Figure 2). (a) Detail of the H0228 and H0241 nadir images (22.4 m pixel^{-1}). (b) Location of valley networks (gray lines) detected automatically in the HRSC DEM. The widest corresponds to the main tributary Jup-Jdw. Thick black lines mark the location of transverse topographic profiles across the main tributary Jup-Jdw. The contour line interval (thin black lines) is 200 m. (c) The 3-D view of this area showing the radial pattern of valley networks around the central hill.

for sources. However, valleys differ in geometry, with a trapezoidal shape in the northern part and an open V shape in the central and southern parts.

3.2. Valley Networks East of the Huygens Impact Crater

[39] The Huygens 475-km-diameter impact crater is a major geological feature northwest of Hellas basin in the Iapygia quadrangle of Mars (Figure 11a). This region is mainly old, hilly and cratered upland terrain [*Schaber*, 1977], dated to the Noachian Period [*Tanaka*, 1986; *Greeley and Guest*, 1987] interrupted only by a few ridged plains of the Early Hesperian Epoch [*Tanaka*, 1986; *Greeley and Guest*, 1987].

3.2.1. Morphometric Analysis at the Regional Scale

3.2.1.1. HRSC Image Analysis

[40] The HRSC camera acquired a nadir image, on the eastern rim of the Huygens impact crater, centered at 22.7°S–61.6°E, during the H0532 orbit. We limited our study to the northern part of the H0532 image between 12°S and 21°S (Figure 11b). Because of the acquisition geometry of the Mars Express orbiter during this period, the panchromatic images have a low spatial resolution of 37.9 m pixel^{-1} for the nadir image, 70.6 m pixel^{-1} for the stereo1 image, and 99.4 m pixel^{-1} for the stereo2 image, corresponding to the pixel size at the center of the images. The nadir image has been projected in sinusoidal projection centered at longitude 60°E with a spatial grid of 50 m pixel^{-1} (Figure 11b). Numerous valley networks incised the eastern outer rim of the Huygens impact crater (upper left corner in Figure 11b). They show a well-developed organization with a Strahler order of 4 (Figure 11c) and are characterized by more than 100-km-long, elongated drainage basins oriented parallel to the outer impact rim slope. The valleys vanish eastward into the smooth region dated to the Hesperian Period [*Tanaka*, 1986; *Greeley and Guest*, 1987]. Numerous valley networks debouch into the western side of large, rimless impact craters that apparently acted as terminal depressions (Figure 11, box indicating Figure 14). The inner rim of Huygens impact

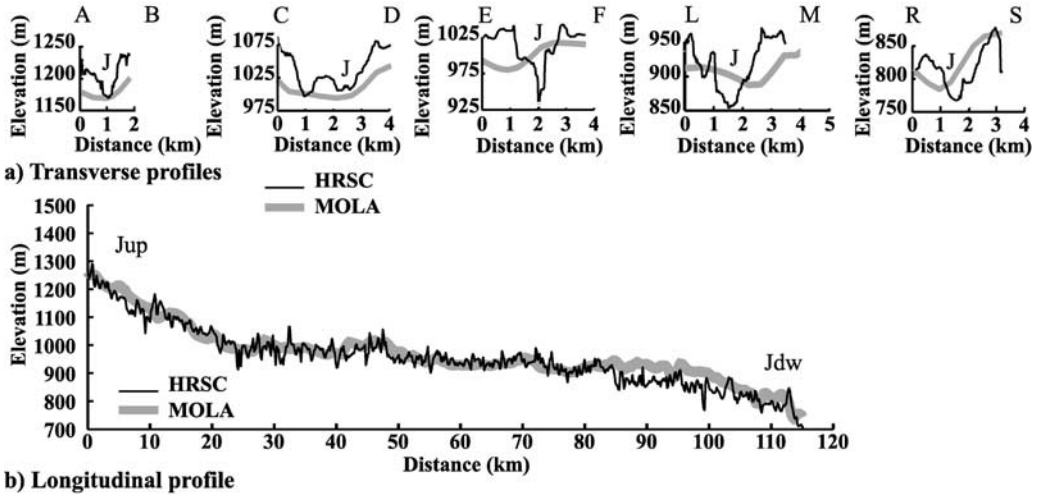

Figure 7. (a) Transverse profiles extracted across the main tributary Jup-Jdw (see Figure 6). Notice that the main tributary J increases in depth and width downstream on the HRSC profiles, and the valley side slopes are twice as steep as those observed in the MOLA profiles. (b) Longitudinal profile of the main tributary Jup-Jdw showing a slightly concave shape.

crater is also incised by smaller drainage basins. A few normal faults and compressional ridges influence the present-day topography, and the tilted blocks are carved by valley networks, implying that valleys locally postdate the tectonic deformation. However, major valleys are deeper when they crosscut the normal fault scarp and the compressional ridge, suggesting that they began their incision during the tectonic uplift. In addition, a few poorly branched valley networks have been developed in ejecta of 50-km-in-diameter degraded impact craters, e.g., the impact crater located at 63°E–13°S (Figure 11).

3.2.1.2. HRSC DEM Calculation

[41] We found 1,801,543 homologous points for which 3-D coordinates have been calculated with a good accuracy (σx = 20.7 m, σy = 30.4 m and σz = 17.6 m) using the triplet of images (one nadir and two stereo). The statistical height error is 26.6 m on each 3-D object point. The points on the interpolated HRSC DEM have a spatial gridding of 250 m pixel^{-1} (Figure 12), a low resolution due to the limitation from the base image resolution and the gaps of homologous points in some regions. Although the distribution of points is heterogeneous, morphologic features are well fit in the hilly region. The regional topography viewed from the HRSC DEM (Figure 12b) and MOLA (Figure 12a) shows that the rim of Huygens crater reaches 3000 m elevation and 2000 m above its flat floor. The northeastern plain stands at 1200 m elevation. The southern area has hilly topography surrounding a plain standing at 500 m in elevation, before declining southward into the Hellas basin. The height offset between the MOLA DEM and the HRSC DEM is relatively high (Figure 12d): MOLA is 100 m higher than the HRSC DEM in the central part, whereas it is 200 m lower in the northern and southern parts. These height offsets can induce local differences in topographic slope. The maximum offset in slope is <0.2°, but this is not negligible when we extract valley longitudinal profiles.

3.2.1.3. Morphometric Analysis of Valley Networks

[42] We extracted valley networks from the MOLA DEM (400 m pixel^{-1}) with a minimum threshold of 250 cells of accumulation flow (Figure 13). A total of 97 drainage basins are located essentially at the outer rim of Huygens crater and on hills surrounding the southern plains. Drainage basins cover small areas, with an average area of 180 km^2 (Tables 1 and S3). These basins are relatively elongated and parallel to the slope. They are incised by a few tributaries (<4) corresponding to those observed on the HRSC image. In MOLA, the drainage density ranges from 0.02 to 0.22 km^{-1} with a maximum Strahler order of 3 (Tables 1 and S3). For example, the widespread drainage basin V covering 2953.76 km^2 is incised by 22 valleys up to a Strahler order of 3 and with a total length of 252 km (Figure 13). The drainage density is 0.09 km^{-1} close to the regional average (Table 1).

[43] By comparison, 129 drainage basins have been detected automatically with a minimum threshold of 400 cells of accumulation flow in the HRSC DEM at grid of 250 m pixel^{-1} (Figure 13). Their mean surface area is quite similar (160 km^2) to that of basins detected in MOLA (Tables 1 and S4). The shape of basins in the HRSC DEM remains elongated and controlled by the regional slope. The mean number of tributaries does not change in each basin (<4), and the drainage density is between 0.02 and 0.23 km^{-1} with a maximum of Strahler order of 4 (Table 1). The drainage basin V increases in surface area compared to MOLA, with 3915.13 km^2 due to improved resolution of the drainage divide in the HRSC DEM (Figure 13). A total of 44 valleys incise the basin with a Strahler order of 4. The total length of valleys being 576.66 km, the drainage density increases significantly up to 0.15 km^{-1} compared to that found in MOLA.

[44] As regards the manual mapping, the drainage basin V has a surface area close to that previously determined with the HRSC DEM, and it is incised by 87 valleys arranged with a fourth-order stem. The total length of tributaries is 650.52 km, giving it a drainage density of 0.17 km^{-1}, which is very close to that found with the HRSC DEM. Thus, the best spatial resolution of the nadir image does not allow us to significantly increase the drainage

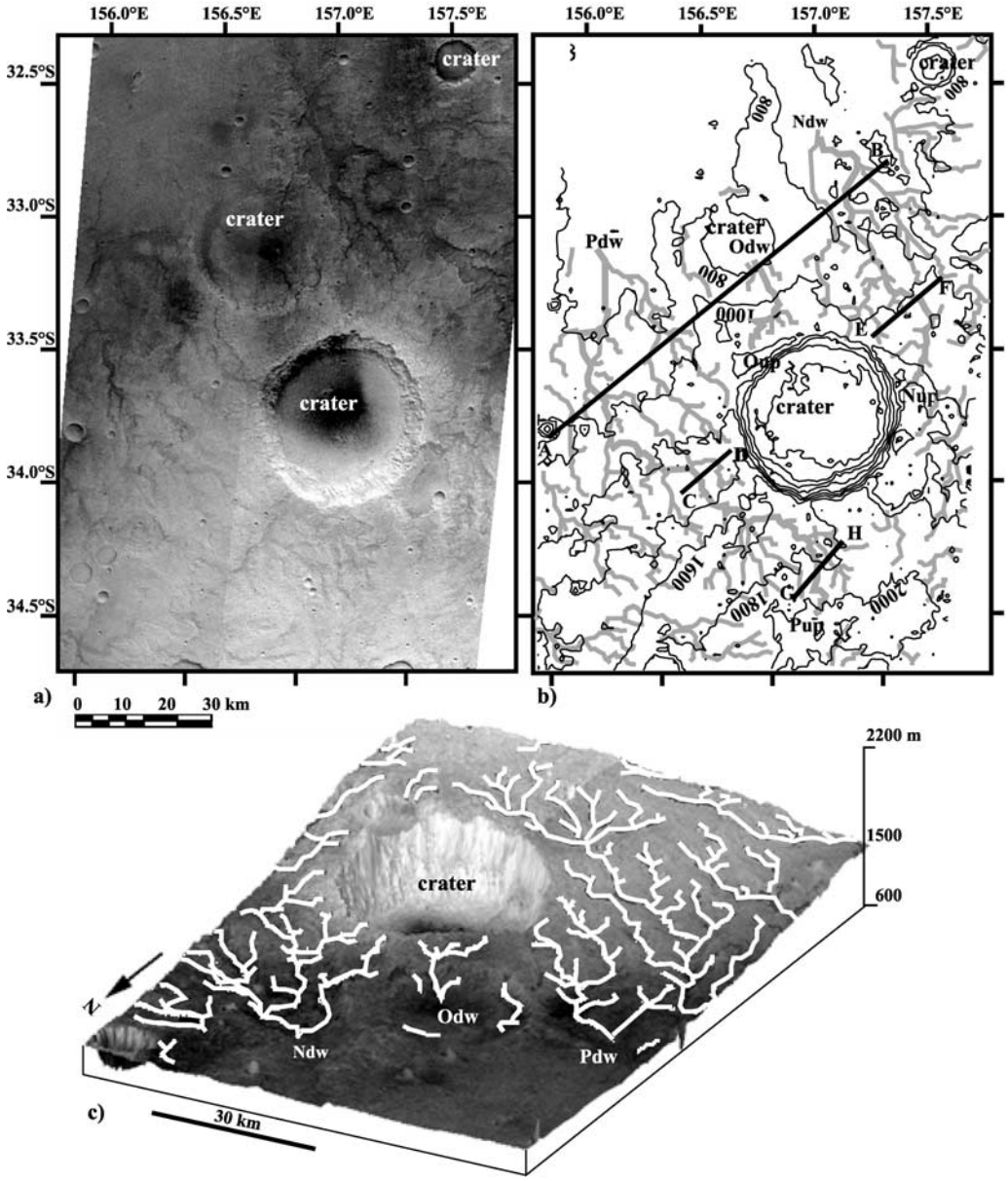

Figure 8. Detailed study of the southern part of the Aeolis region (Figure 2). (a) Detail of the H0228 and H0241 nadir images (22.4 m pixel^{-1}). (b) Location of valley networks (gray lines) detected automatically in the HRSC DEM. The thick gray lines labeled Ndw-Ndw, Oup-Odw, and Pup-Pdw correspond to the main tributaries of N, O, and P valley networks. Thick black lines mark locations of transverse topographic profiles. The contour interval (thin black lines) is 200 m. (c) The 3-D view of valley networks distributed radially around the hill superimposed on the HRSC image. Note the valley network O that crosscuts the old infilled impact crater.

density for this drainage basin. The highest drainage density is 0.29 km^{-1} for the drainage basin F in the HRSC image. Compared with the HRSC DEM at the grid scale five times smaller, the drainage density is increased by a factor of 2 in the manual mapping, with a maximum of 0.29 km^{-1}, but the maximum Strahler order remains equal to 4.

[45] In summary, the HRSC DEM gives a slight improvement in the characterization of drainage basins compared to MOLA, but the ratio of spatial resolution between MOLA and HRSC is only 1.8. The characterization of drainage basins from the HRSC DEM remains low with respect to that extracted from the manual mapping.

3.2.2. Detailed Analysis of Drainage Basins Near the Huygens Impact Crater

[46] We describe two different areas of valleys on the HRSC image (Figures 14, 15, 16 and 17). In each area, we describe the valley networks and discuss the longitudinal and transverse profiles extracted from MOLA and the HRSC DEMs.

3.2.2.1. NE Rim of Huygens Impact Crater

[47] In this area (Figures 11 and 14), three valley networks developed on the eastern topographic slope before debouching into the 40-km-in-diameter rimless, flat-floored impact crater. Valley networks have a relatively dendritic

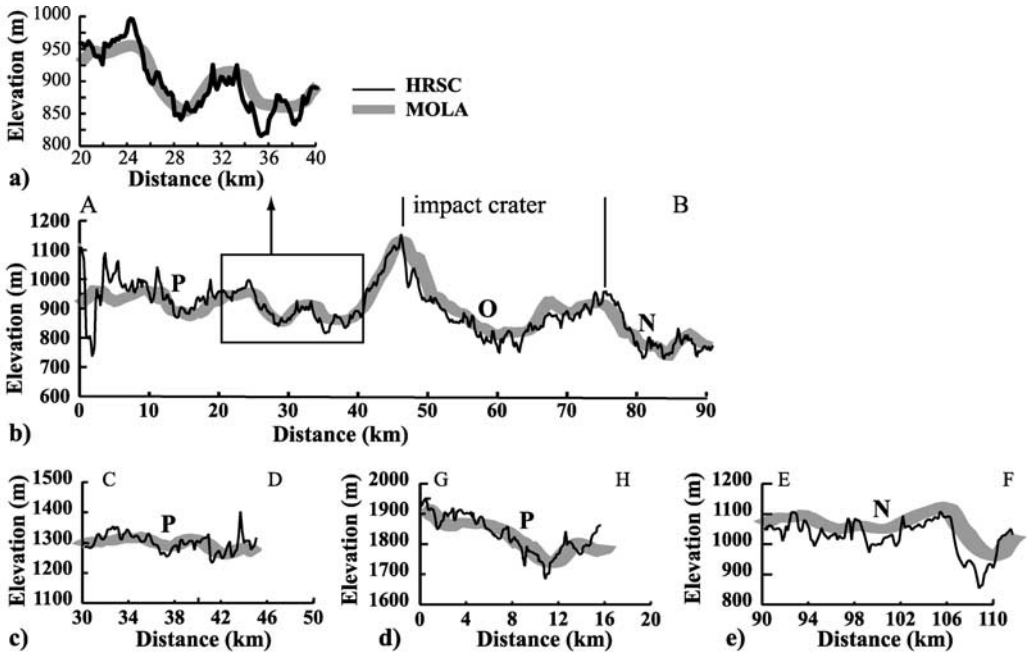

Figure 9. Transverse profiles across the main tributaries of valley networks labeled N, O and P in Figure 8. (a) Detail of the box in Figure 9b with vertical and horizontal exaggeration. Notice that the HRSC topography detects two valleys where one is found in MOLA between 36 and 40 km. (b) Transverse profile A-B across the three valley networks N, O, and P. (c) and (d) Transverse profiles across the tributary P. Notice that the valley P deepens downstream (50 m in GH, 80 m in CD and 100 m in AB). (e) Transverse profile across the tributary N.

pattern with numerous tributaries starting at different elevations. The southern valley network has a change in pattern close to its outlet, with a circular, concave drainage basin (Figure 14, near cross section NS4). The superposition of the valleys automatically detected in the HRSC DEM on the HRSC nadir image viewed in 3-D (Figure 14c) shows that valleys follow the present-day topographic slope.

[48] The three N-S cross sections display the same open V shape in MOLA and in the HRSC DEM (Figure 15a). In this case, the HRSC transverse profiles do not give more information than do those from MOLA. Only the major tributaries are detected with a width >1 km and a depth of ~100 m (Figure 15a). In both data sets, the width and depth of major valleys increase downstream, e.g., valley F reaches 3 km in width and 180 m in depth at its outlet.

[49] The longitudinal profiles reveal the roughly 100-m-height offset between MOLA and the HRSC DEMs (Figure 15b). As the height offset is nearly constant along the longitudinal profiles, there is no effect on the topographic slope between the two data sets. The longitudinal profiles are straighter upstream and transition to a convex-up profile or have a topographic step where they crosscut the crater rim. The topographic step is far upstream for the longitudinal profile I, and it corresponds to the topographic limit of the circular, concave drainage basin near the outlet Idw (Figure 14a). The downstream convex-up profile is due to a knickpoint that is partially due to blind tectonic structures or lowering of base level (Figure 15b).

3.2.2.2. Eastern Rim of Huygens Impact Crater

[50] In the eastern part of Huygens crater rim (Figures 11 and 16), major E-W trending normal faults bounded a E-W graben, and a NW-SE trending ridge, likely a thrust fault formed a topographic scarp facing northeastward. First, branching valley networks developed on the backside of the ridge and crosscut the southern normal fault debouching into the graben (Figure 16, see, e.g., the main tributary Vup-Vdw). Valley heads stand at different elevations and the highest are at 2700 m. Second, two valley networks developed on opposite sides within graben on the old rim of Huygens impact crater (Figure 16, P and Q drainage basins). All of these valley networks formed after the graben, because they crosscut it. The 3-D view displays the deep incision when valleys crosscut the ridge scarp and the divide between P and Q drainage basins inside the graben (Figure 16c).

[51] The transverse profiles across drainage basins P and Q are quite similar in the two data sets, with a minimum valley depth of 100 m (Figure 17a, NS1 to NS2). However, these cross sections correspond more to topographic profiles across drainage basins P and Q than to individual valleys. It is difficult to observe the geometry of distinct valleys incising the drainage basins at the 250-m spatial grid of the HRSC DEM. For the topographic profiles across the drainage basin V, valleys show different shapes, especially for the NS4, in which more valleys are detected with a minimum depth of 50 m in the HRSC data set (Figure 17a). We notice that the valley depth remains quite constant with a tendency to decrease downstream. This characteristic could be the result of either (1) a late filling of the valley downstream by dust or volcanism or (2) local vertical adjustment of incision in the upstream direction in response to tectonic uplift during the wrinkle ridge formation.

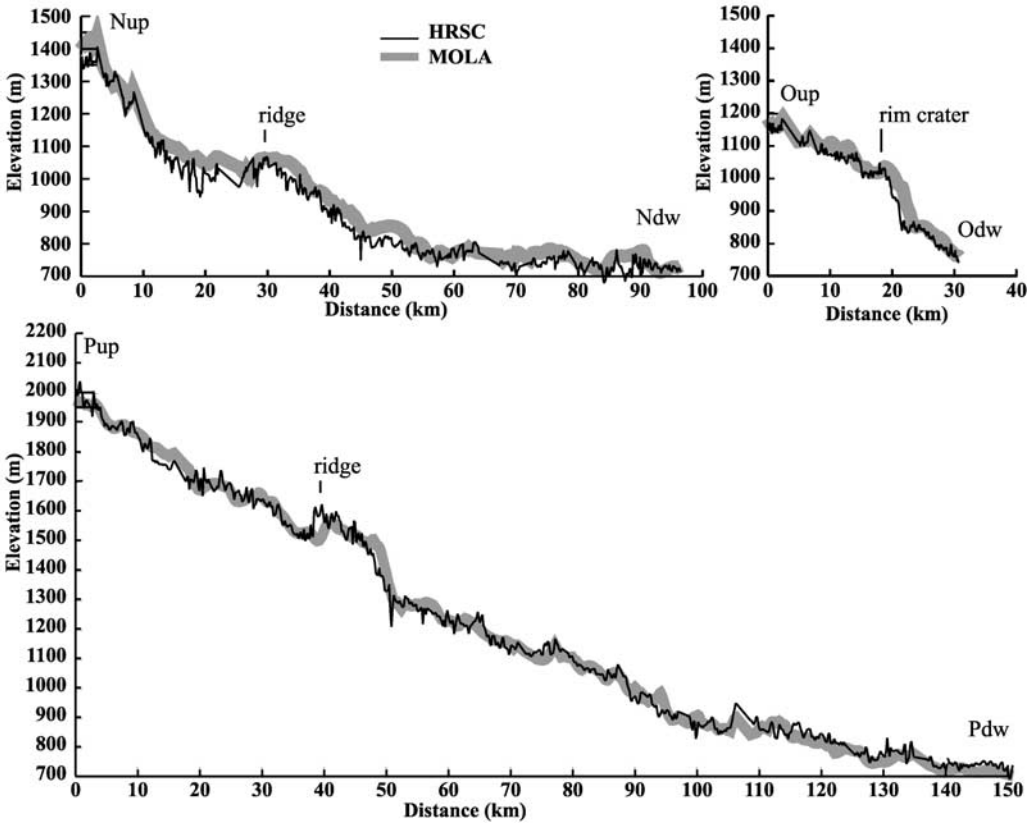

Figure 10. Longitudinal profiles of different major tributaries viewed in Figure 8. Except for the topographic profile Oup-Odw that crosscuts the old impact crater rim, the others have a concave shape, suggesting that they reached an equilibrium. Note that a late ridge deformed the previous valley profile.

[52] The shape of longitudinal profiles remains quite similar, but the irregular height offset introduces some difference in slope measured at the local scale, e.g., the longitudinal profile P (Figure 17b), demonstrating that profiles must be interpreted with caution in these areas. The longitudinal profile V seems graded with a concave-up shape, except for the topographic trough in HRSC data at a distance of 95 km. This trough corresponds to the toe of a wrinkle ridge (8 km eastward of NS5, Figure 17b) where several tributaries connect in the HRSC nadir image (Figure 16a). In contrast, the longitudinal profiles P and Q display a convex-up shape (Figure 17b). The divide between the two drainage basins P and Q stands at 2200 m elevation, which is 500 m lower than the valley heads of the valley network V.

3.3. Valley Networks in the Echus Region

[53] The studied area is located on the plateau at the west of the Echus Chasma canyon (81–82.5W, 0–5°N, Figure 18a). Valley networks were first identified in this area from their distinct thermal properties on THEMIS images [*Mangold et al.*, 2004a, 2004b]. The valleys incised the Late Hesperian plateau [*Tanaka et al.*, 1992; *Mangold et al.*, 2004a, 2004b] and are buried by Amazonian lava flows to the north of the Echus plateau. These valleys are interesting because (1) the incised lithology is different from old cratered highlands located in the Aeolis region and the east Huygens crater and (2) the age of valley formation is younger than in the two previous studied regions.

3.3.1. Morphometric Analysis at the Regional Scale

3.3.1.1. HRSC Image Analysis

[54] Three orbits, 97, 920, and 2204, cover this area. We used only the HRSC H2204 image, because it is the only one that provides geomorphic details with a spatial resolution of ~20 m pixel^{-1} (Figure 16b). The studied area extends between 2°N and 2°S (Figure 18c). Although the H2204 nadir image shows sharp changes in albedo, it is possible to recognize, on each side of the Echus canyon, shallow valley networks incising widespread areas that extend more than 200 km along the Echus Chasma western plateau [*Masson et al.*, 2004, 2005c; *Mangold et al.*, 2004a, 2005a, 2005b]. In the central part of the H2204 nadir image, valley floors appear bright in contrast to the nominally dark bedrock, because they are partially filled by relatively light-toned deposits. It is more difficult to discern valleys to the eastern edge of the image because of the thick, bright deposits. Valley networks are not restricted to the locations where they have been observed in the THEMIS images [*Mangold et al.*, 2004a]. They display two patterns: dendritic in the northern part of the H2204 image and parallel in the southern part, suggesting that the regional topographic slope controlled their organization [*Mangold et al.*, 2004a, 2004b]. In addition, valley networks appear well developed throughout their respective watersheds and have a significant headward extension with Strahler order up to 5 at HRSC resolution (Table 1) [*Mangold et al.*, 2007, 2008; *Ansan et al.*, 2007a, 2007b].

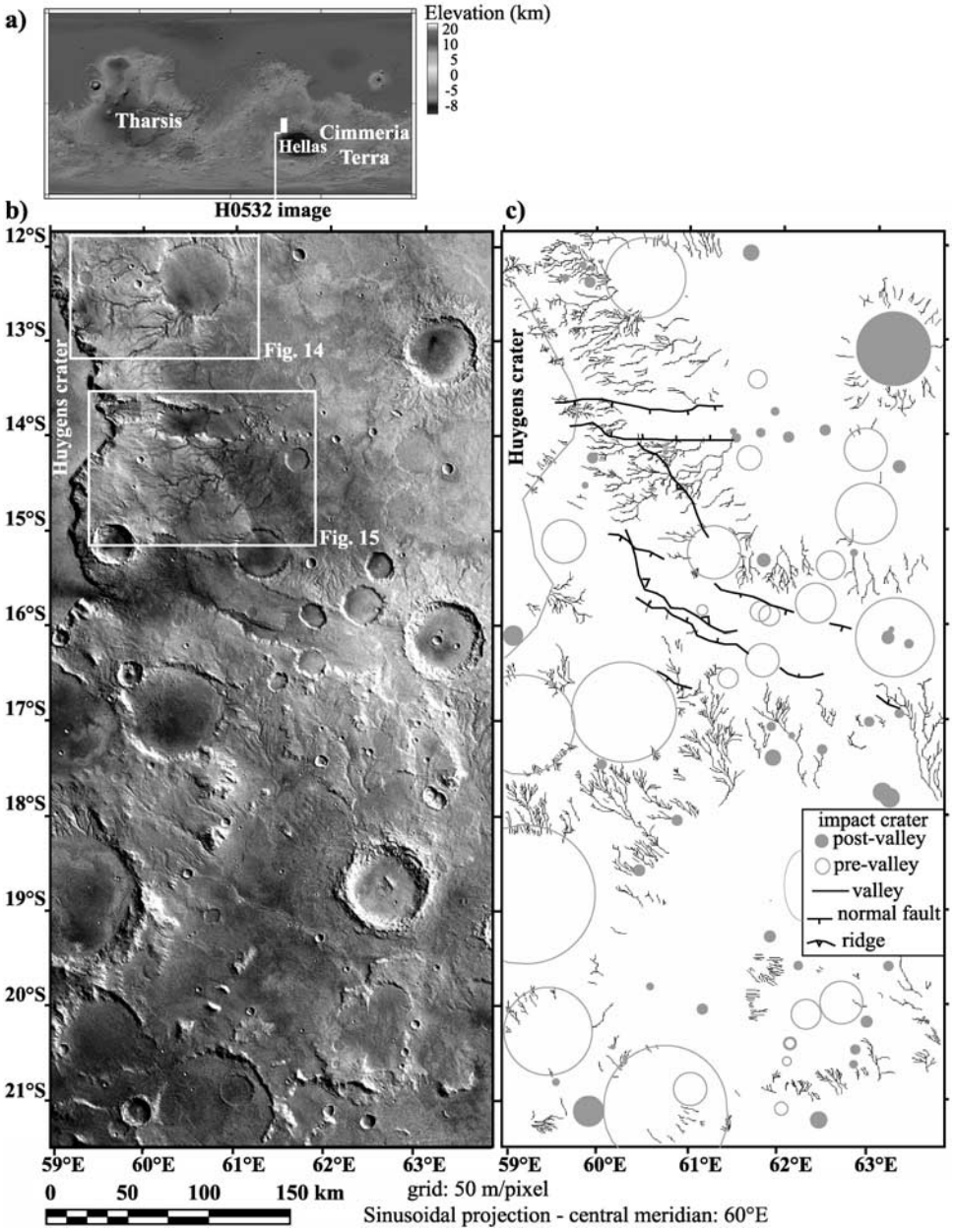

Figure 11. The eastern rim of Huygens impact crater. (a) Location of the H0532 HRSC image on a MOLA map, north of the Hellas basin. (b) H0532 nadir image at 50 m pixel^{-1}. White boxes correspond to the location of Figures 14 and 15. (c) Map of valley networks incising the outer rim of the Huygens crater, created manually using classic photointerpretation methods. Note that old impact craters are crosscut by valley networks.

3.3.1.2. HRSC DEM in the Echus Plateau

[55] The triplet of H2204 images has a spatial resolution of respectively 16.7, 33.9, and 38.9 m pixel^{-1} at the center of nadir and stereo images. A total of 2,108,364 homologous points have been found using these images (Figure 19c) and the exterior orientation data. Their 3-D object points have a relatively good accuracy in x and z Cartesian coordinates (σx = 19.0 m and σz = 17.2 m) but a very poor accuracy in the y coordinate (σy = 53.9 m). Because of this bad accuracy in y coordinate, the mean statistical height error is 53.4 m on each 3-D object point. However, the height error is locally often less than 20 m from point to point, leading to the identification of topographic features much less than 50 m high.

[56] Owing to the large number of 3-D object points found, we chose to generate a DEM with a spatial grid size of 50 m in sinusoidal projection centered at longitude 85° E. The spatial distribution of points is quite homogeneous on each side of the Echus canyon, except for the plateau located north of 0.5°N, where numerous pixels are empty of points. This latter area corresponds to the homogeneously smooth, bright area in H2204 images (Figure 19b), where the matching is inefficient. The sides of the Echus canyon are also poorly sampled. Despite this caveat only 30% of the

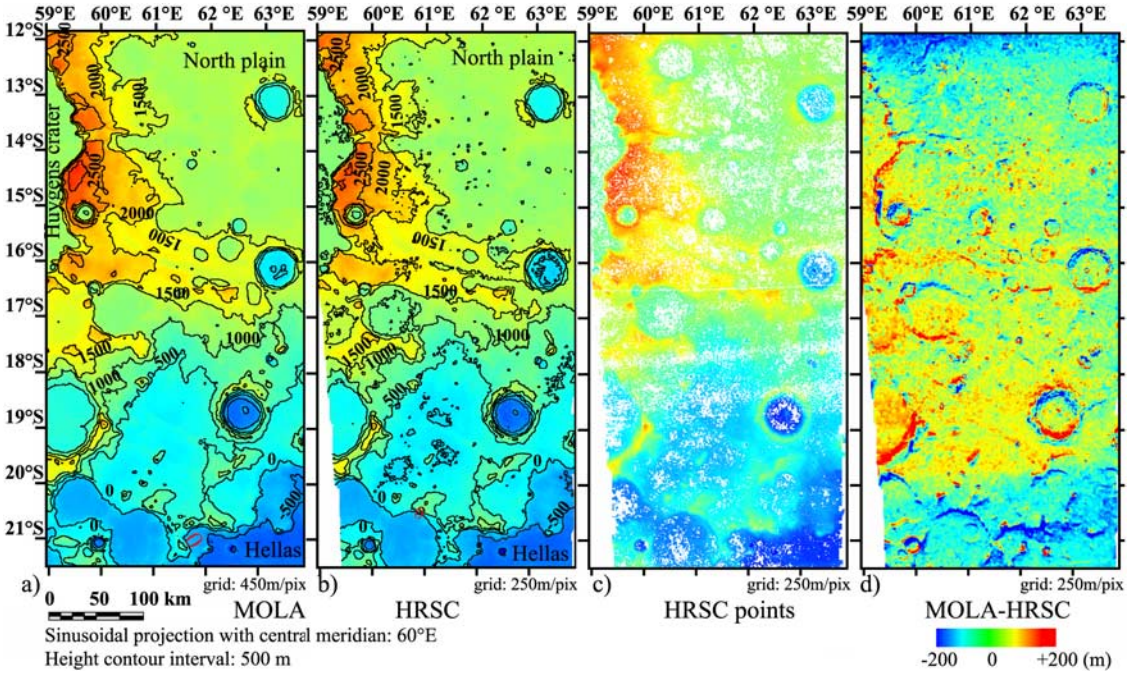

Figure 12. (a) MOLA topographic map at 450 m pixel^{-1}, showing the Huygens crater rim at 3000 m in elevation. The northern plain is separated from the Hellas basin by an E-W ridge standing at 2000 m in elevation. (b) The HRSC DEM generated from the population of 3-D object points (c) distributed in a regular grid of 250 m pixel^{-1} displays the same relief as MOLA with more details. (c) Note the low population of points in flat areas, e.g., the northern plain and the Huygens crater floor. (d) Vertical offset between MOLA and the HRSC DEM is heterogeneous and relatively large. All maps are in sinusoidal projection centered at 60°E longitude. The contour interval is 500 m.

whole grid is empty, and most of areas with the shallow valley networks are well sampled (Figure 19c).

[57] At the regional scale, the HRSC DEM (Figure 19b) is more detailed than the MOLA equivalent (Figure 19a), except on the sides of canyons and on the northern areas of the Echus plateau at 1500 m in elevation. If we compare the HRSC DEM to the MOLA data, we see that the vertical offset is very low (~25 m) on the whole Echus plateau where we observe small valleys, but the disparity is much more important (up to 150 m) on the sides of the Echus canyons (Figure 19d). For this reason, we consider the HRSC DEM to be valid for the automatic detection of shallow valley networks present on the Echus plateau.

3.3.1.3. Morphometric Analysis in the Echus Plateau

[58] We automatically extracted valley networks from the MOLA DEM with a minimum threshold of 900 cells of accumulation flow (Figure 20). A total of 17 drainage basins have been detected on the Echus plateau and they cover small areas (392 km^2 on average), except that three basins (D, G, I) exceed 1000 km^2 (Tables 1 and S5). Those located on the southern part of the Echus plateau are relatively elongated, parallel to the slope, but drainage basins in the northern part have circular shapes. They often contain a few tributaries (<5) that correspond to the major ones observed in the HRSC image (Figure 18). In MOLA data, the drainage density ranges from 0.03 to 0.15 km^{-1}, with a maximum Strahler order of 3 (Table 1). For example, the widespread drainage basin D covers an area of 1459.50 km^2, in which four valleys are arranged with a network Strahler order of 2 (Figure 20). The total length of valleys is 73.44 km, giving a drainage density of 0.05 km^{-1}. The highest drainage density found using MOLA is in the drainage basin L, where three valleys have been detected. However, this drainage density must be taken with caution, because it does not include the totality of the drainage basin, and the detected valleys are poorly visible in the HRSC image due to the dust-sand mantle in this area.

[59] In contrast, 45 drainage basins have been detected automatically with a minimum threshold of 9000 cells of accumulation flow in the 50 m pixel^{-1} HRSC DEM (Figure 20). The drainage basins covering a mean surface area of 71 km^2 are smaller than those found in MOLA (Tables 1 and S6), whereas the widespread basins (D, G and I) detected in MOLA have the same surface area in the HRSC DEM. In the latter, the number of tributaries increases significantly in each basin (>5), and the drainage density is in the range of 0.04 to 0.30 km^{-1} with a maximum Strahler order of 4 (Table 1). The tested drainage basin D has the same area (1463.30 km^2) as in MOLA, but the number of tributaries in the HRSC DEM increases significantly with seven times more tributaries than in MOLA. The tributaries in the HRSC basin D have a maximum Strahler order of 3, and a total length of 236.60 km, leading to a drainage density of 0.16 km^{-1}, that is three times higher than in MOLA. The highest drainage density of 0.30 km^{-1} in the HRSC DEM is found in the drainage basin C5, whose surface area decreases significantly because of the detection of surrounding drainage basins (Figure 20).

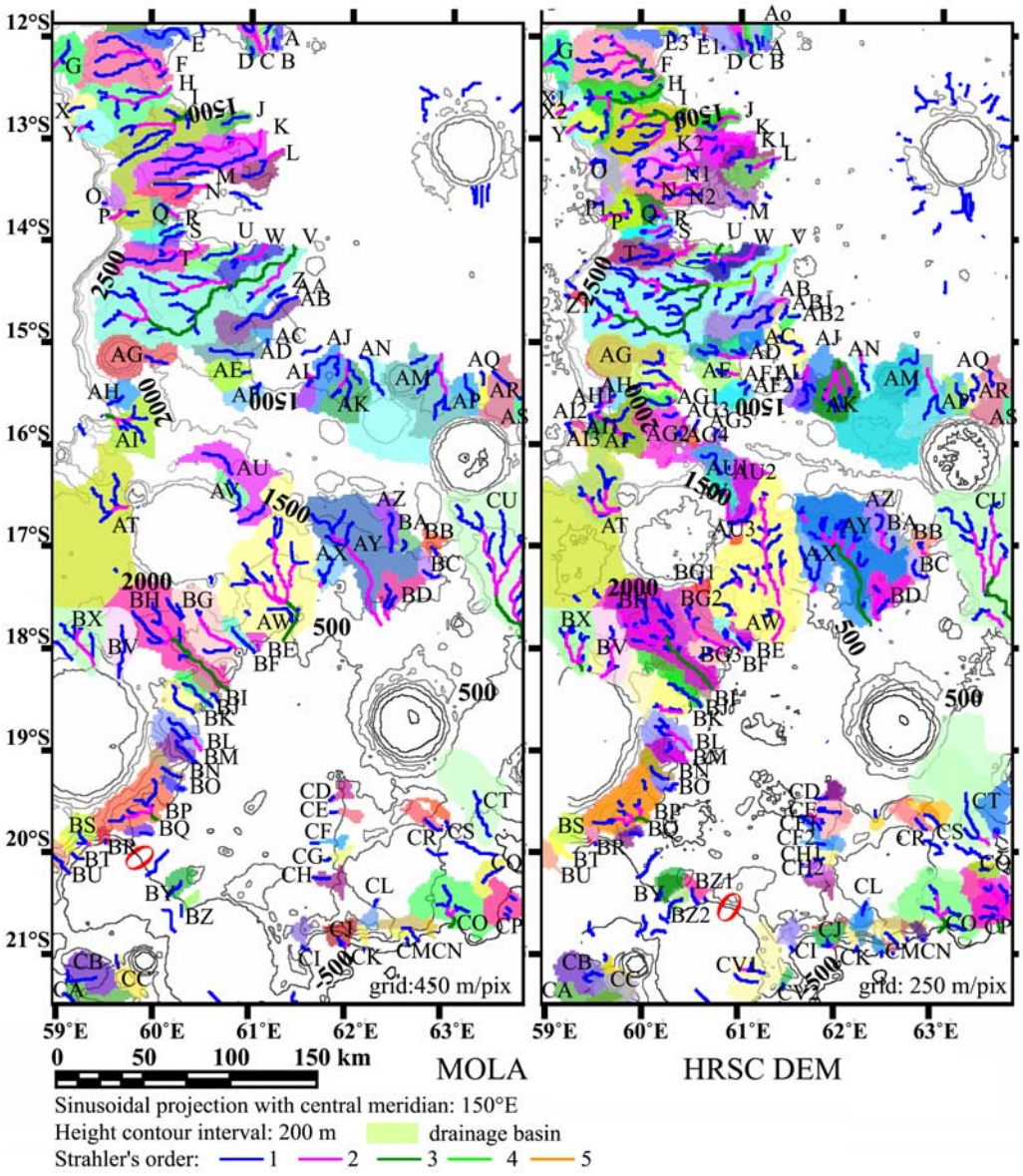

Figure 13. Comparative maps of valley networks detected automatically in MOLA and the HRSC DEM, which have different spatial resolution. Drainage basins are bounded by their colored area and assigned a letter. Each Strahler order is identified by a color. More basins have been detected in the HRSC DEM than in MOLA (see text for details).

[60] Regarding the manual mapping, drainage basin D (defined by the highest points surrounding the drainage area in the HRSC DEM) differs from the one apparent in the HRSC image (Figure 18). Indeed, the drainage basin D defined from the HRSC DEM covers a large area and contains three valley networks, which are spaced across an area (0°N–81°15′W) in the HRSC image where the valleys are difficult to map due to the dust and sand mantle. If we consider that the three valley networks form one catchment area, then we can characterize the morphometry of this drainage basin D. A total of 263 valleys with a network Strahler order of 5 incise 843.37 km, giving a drainage density of 0.58 km^{-1}, twice that found in the HRSC DEM. In this case, we defined three drainage basins, and the highest drainage density (1.3 km^{-1}) is found for the southern drainage basin that has a Strahler order of 5.

[61] Mapping of the western part of the Echus plateau has fewer valleys (Figure 18) compared to the automatic mapping from altimetry (Figure 20). Although at least one valley exists on the HRSC image, we consider that they are very shallow and at the limit of subjective interpretation. For this reason, we did not map this region. The consequence is a drop in the estimate of drainage density from the nadir image in the 45 drainage basins detected inside the HRSC DEM. However, the mean drainage density in this manual map is 0.35 km^{-1}, twice as high as that found in the HRSC DEM (Table 1). In this manual mapping the highest drainage density is 0.80 km^{-1} in the drainage basin B1 outlined in the HRSC DEM (Figure 20).

[62] If we compare the morphometric analysis of the Echus plateau from the manual mapping of the nadir HRSC image (20 m $pixel^{-1}$) to the automatic mapping of the

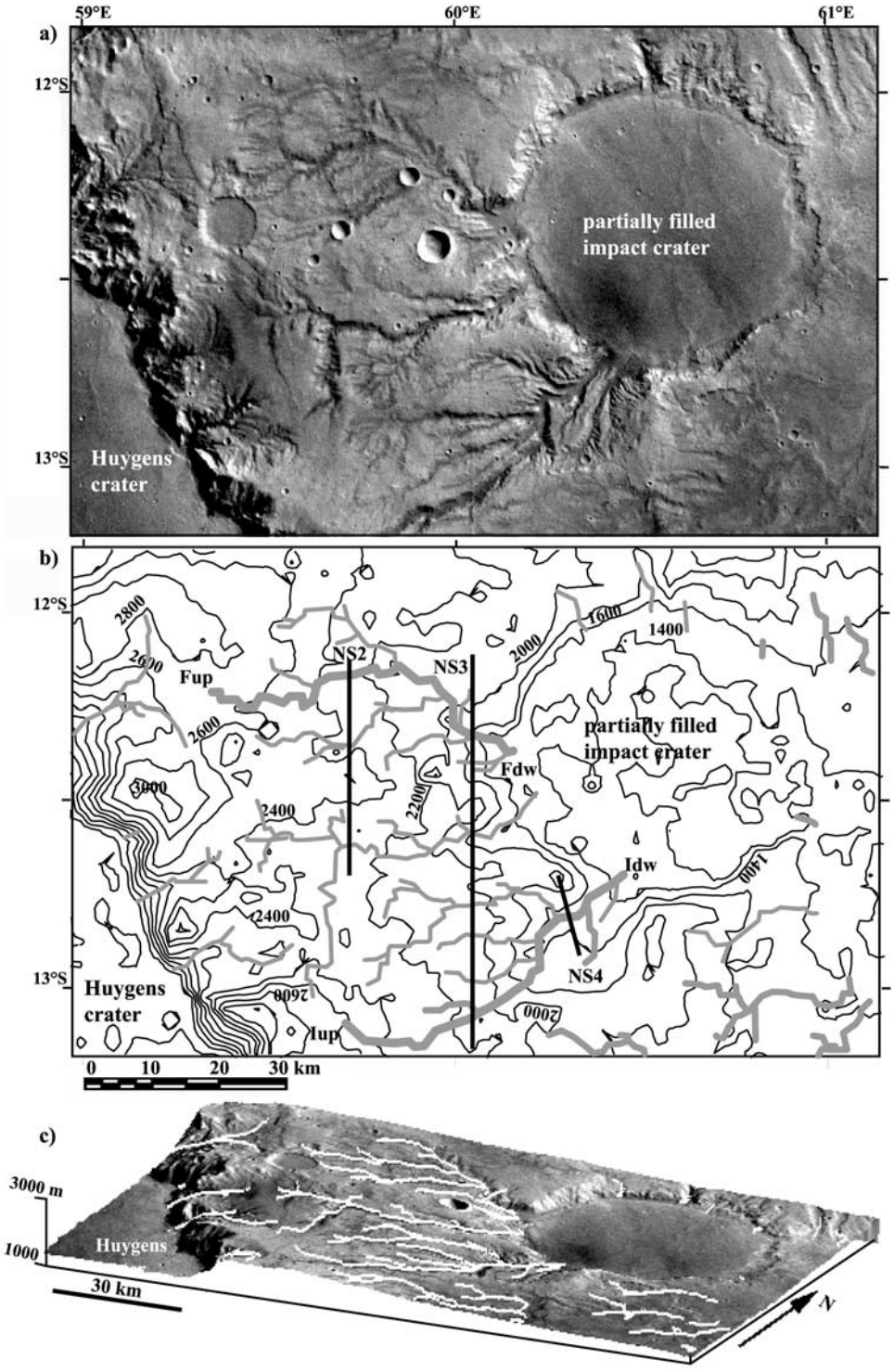

Figure 14. Detailed study of the northeastern rim of Huygens impact crater. (a) Detail of the H0532 nadir image (50 m pixel^{-1}), where valley networks incise the inner and outer sides of the Huygens rim. Valley networks are relatively dense and debouch into the partially filled impact craters. Notice that blind thrust faults often control the orientation of valleys. (b) Location of valley networks (gray lines) detected automatically in the HRSC DEM overlaid on a contour map with 200-m interval. The thick gray lines are the main tributaries of valley networks F, H, and I. Thick black lines mark the locations of transverse topographic profiles seen in Figure 15. (c) A 3-D view of this area.

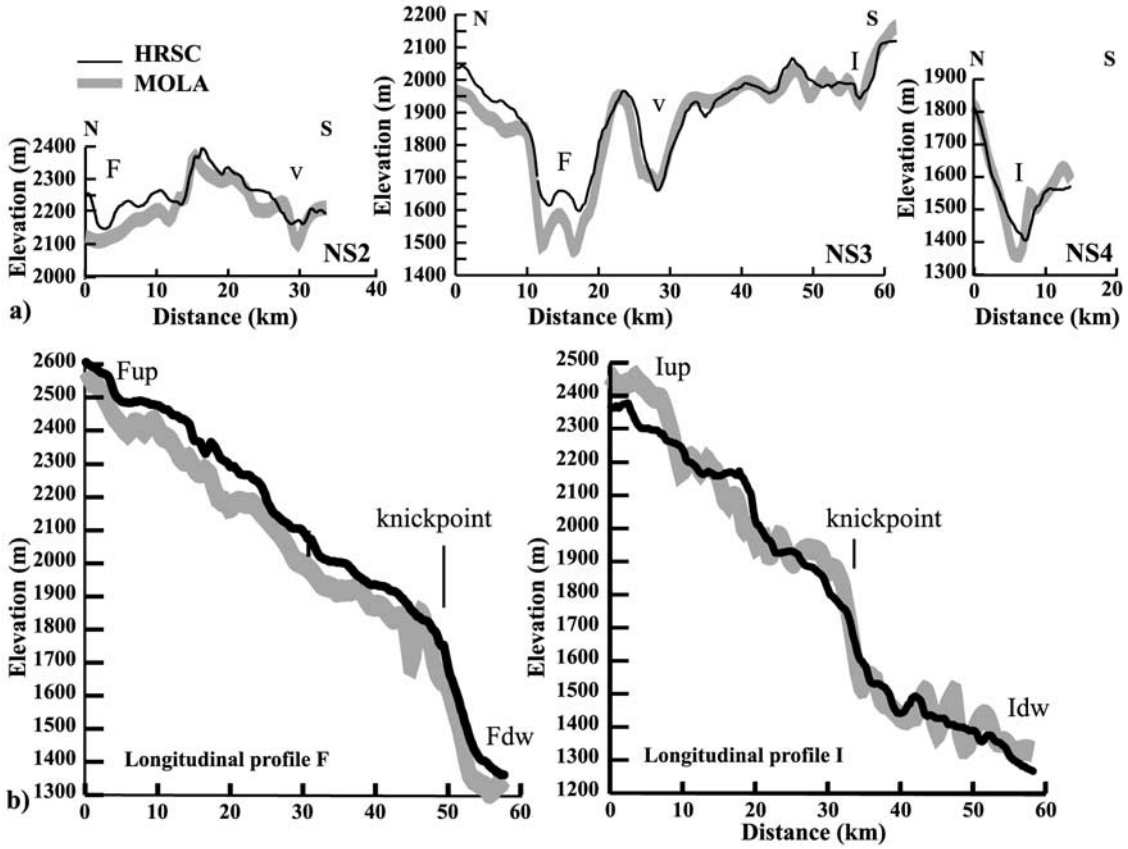

Figure 15. (a) Transverse profiles across the main tributaries observed on the outer rim. Depths of valleys increase downstream when they debouch into the filled impact crater (NS3 and NS4). The v corresponds to the deep valley oriented E-W observed on the HRSC image (Figure 14). (b) Longitudinal profiles of tributaries F and I seen in Figure 14. They have relatively straight profiles except where they crosscut the old rim of a filled impact crater (knickpoint).

HRSC DEM at less than half the resolution (50 m pixel^{-1}), we find that the drainage density is significantly increased in manual mapping up to 0.80 km^{-1} with a maximum Strahler order of 5 [*Mangold et al.*, 2007, 2008]. Thus, the HRSC DEM gives a strong improvement in the characterization of drainage basins compared to MOLA, but it remains inferior to the manual mapping from the HRSC imagery, in which drainage basins are easily defined.

3.3.2. Detailed Analysis of Drainage Basins in the Echus Plateau

[63] When we superimpose valley networks detected automatically from the HRSC DEM on the H2204 nadir image viewed in 3-D (Figure 21), we notice that tributaries fit well with their locations in the image, and that the major tributaries are connected to the amphitheater-shaped heads of the Echus Chasma tributary canyons. Exceptions exist with the valleys in the southwestern part of the image. These valleys were found automatically from the DEM and are located in the part of plateau where valleys are difficult to map from the image only. The DEM topography shows valleys, but without a visual confirmation, we cannot be sure of their existence at every location. All valleys follow the current topography, which suggests that no significant tectonic or volcanic event has occurred after their formation.

[64] If we focus on the southern end of the largest tributary canyon (Figure 22), valley networks have a subparallel pattern where the regional slope is 1.5° to the north, whereas a more dendritic pattern is predominant on the Echus plateau where the northward regional slope is <1.0°. All main tributaries connect to the heads of the large tributary canyons, which suggests a coeval evolution of both landforms.

[65] Six E-W topographic cross sections have been plotted across the drainage basin D in which the main tributaries crosscut the different regional topographic slopes before joining the Echus canyon heads (Figures 22 and 23). The mean height offset between MOLA and HRSC is very low (<30 m), except in the upstream area where it reaches 100 m (Figure 23a, EW6 profile). The main tributary D increases in depth and width along the downstream direction until the EW3 cross section: depth increases from 100 m to 250 m, and width ranges from 1 km to 5 km (Figure 23a). Notice that the depth increases where the main tributary crosscuts the inner scarp of a degraded impact crater (Figure 23a, EW4 profile). Inside the crater, which is partially filled by a dust-sand deposit, the main tributary D decreases in depth and width, but it remains detected by automatic routine in the HRSC DEM.

[66] The main tributary C has the same downstream behavior (Figures 22 and 23). In comparison to the manual mapping of valleys, only the major tributaries deeper than 50 m were detected in the HRSC DEM as the tributaries located eastward from the tributary D (Figure 23a). Despite

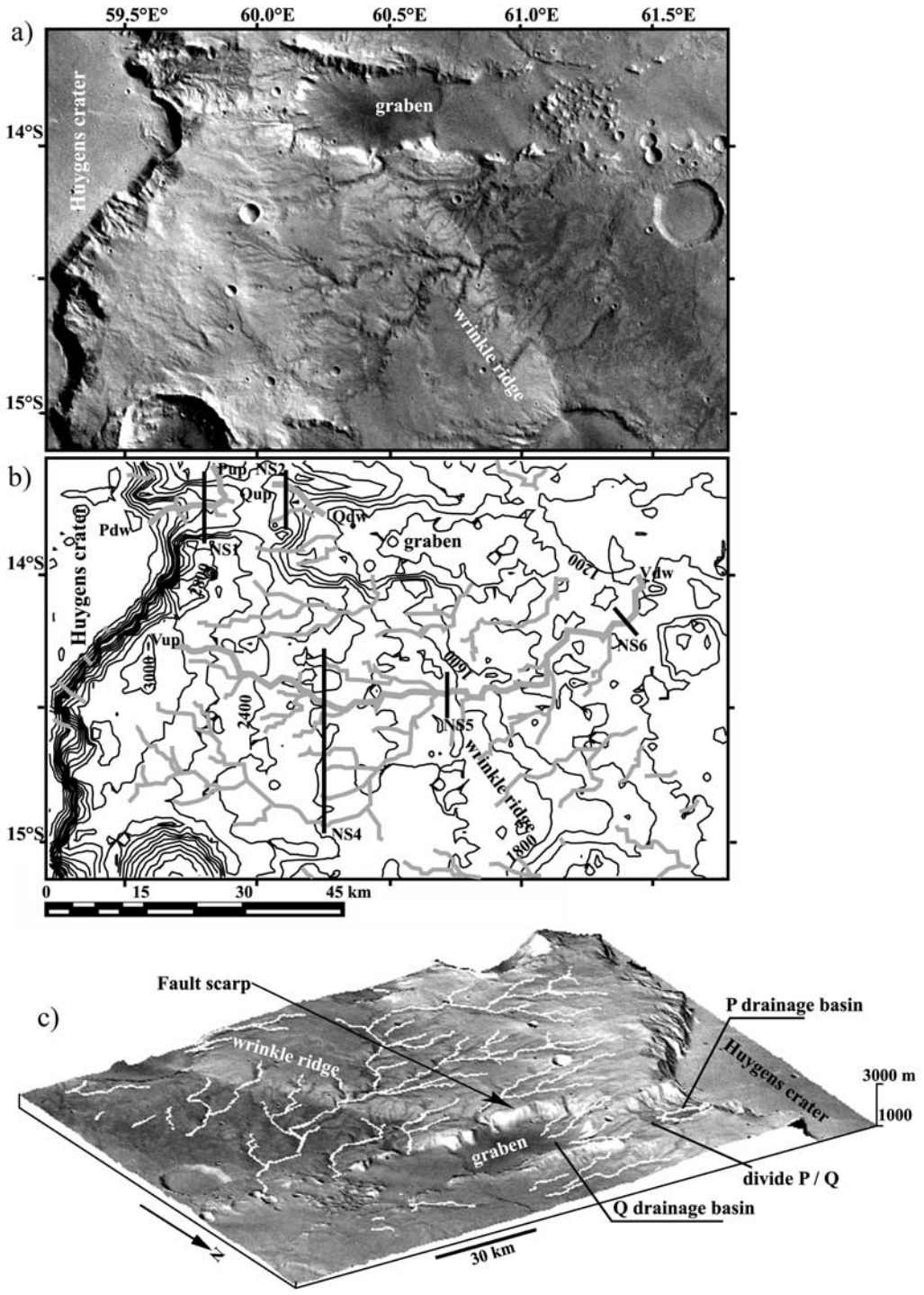

Figure 16. Detailed study of the eastern rim of Huygens impact crater. (a) Detail of the H0532 nadir image (50 m pixel^{-1}). Numerous valley networks incise both the inner and outer sides of the Huygens rim. Note that the southern ones crosscut the NW-SE trending wrinkle ridge. North of 14°S, an E-W oriented graben has two opposing drainage basins, where the divide is located along the 60°E meridian. (b) Location of valley networks (gray lines) detected automatically in the HRSC DEM superimposed on the HRSC height contour lines with 200-m interval. The thick gray line corresponds to the longitudinal profiles of the main valley networks seen in Figure 17. Thick black lines correspond to the locations of transverse topographic profiles seen in Figure 17. (c) The 3-D view of the HRSC image overlaid on the HRSC DEM. Note that valleys deepen as they crosscut the wrinkle ridge.

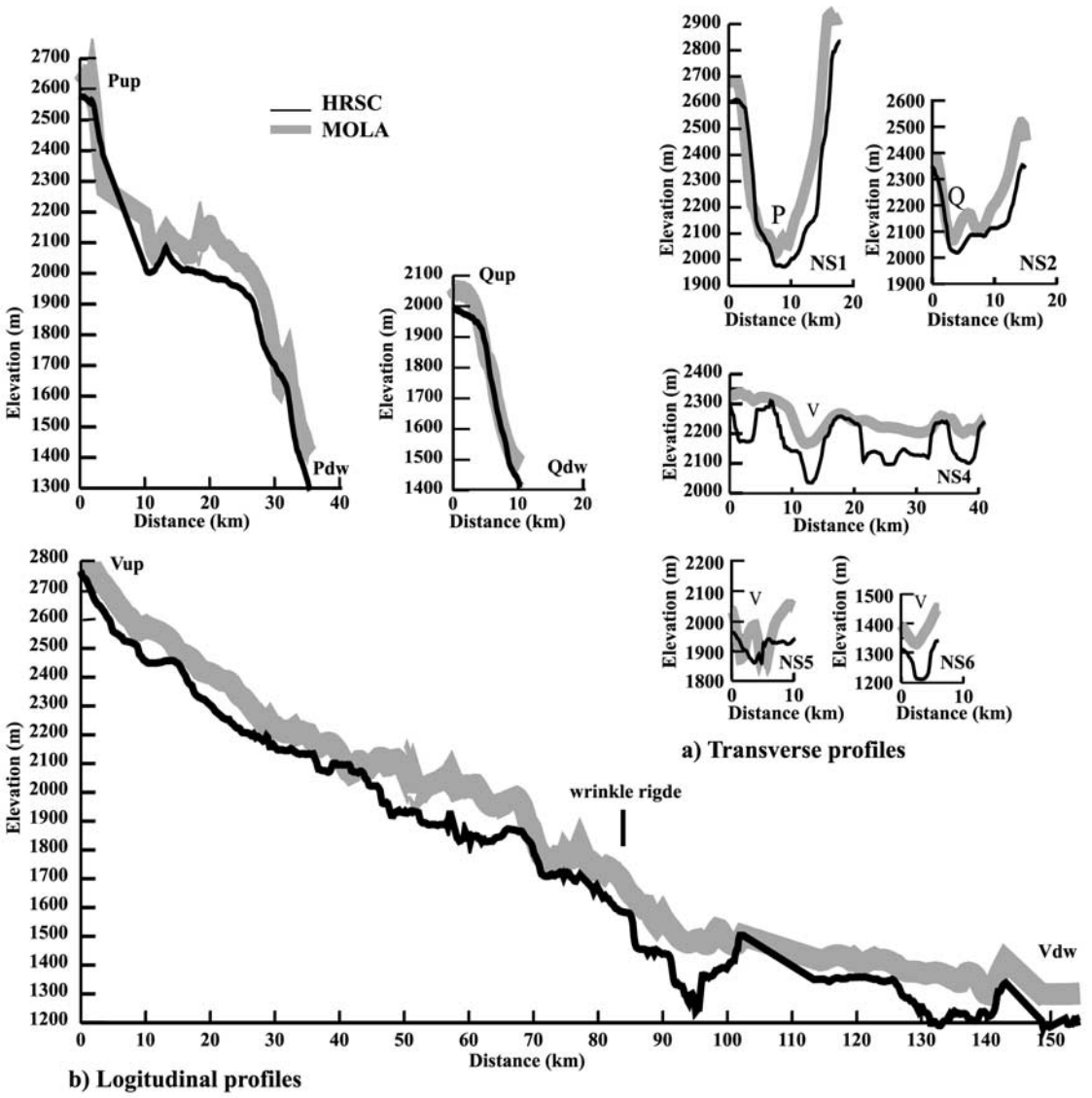

Figure 17. (a) Transverse profiles with locations noted in Figure 16. The profiles NS1 and NS2 display the shape of the drainage basin rather than that of its major valleys, whose depths do not exceed 100 m. In the cross sections along the main tributary V, the valley V diminishes in depth downstream to around 100 m. Note that the HRSC DEM detects six major valleys along the NS4 profile as observed on the HRSC image (Figure 16). (b) Longitudinal profiles of the three main tributaries observed in Figure 16. Except for the profiles P and Q, the valley V has a concave shape that is locally modified by the wrinkle ridge. The convex shape of the two previous profiles could be explained by the relatively young stage of erosion in these two drainage basins compared to the valley networks V.

the low height accuracy of the HRSC DEM on the Echus plateau, it allows us to extract the major tributaries observed in the nadir images, even if they are partially buried by a dust or sand mantle. As the main detected tributaries have depths of 20 to 80 m, we deduce that all smaller valleys visible on the nadir image are very shallow.

[67] The HRSC longitudinal profiles C and D, located on the western Echus plateau, display similar shapes viewed in MOLA data, despite the mean height offset of 50 m (Figure 23b). These two longitudinal profiles are straight, parallel to the regional topography. The longitudinal profile C has a relatively constant topographic slope (0.5°) to the canyon. The profile D has two sharp changes in topographic slope, at 10 km and 55 km from the valley head respectively. The first inflexion point corresponds to the change in topographic slope between the northward sloping region and the Echus plateau, probably due to an E-W tectonic fault. The second inflexion zone corresponds to the 100-m-high inner scarp of an old, degraded and partially filled impact crater (near the EW4 profile in Figure 22).

4. Discussion 1: Improvement of Valleys 3-D Geometry using HRSC DEM

4.1. Strength and Limitations of the HRSC DEM Technique

[68] The quality of the HRSC DEMs strongly depends on the acquisition geometry of the triplet of images that

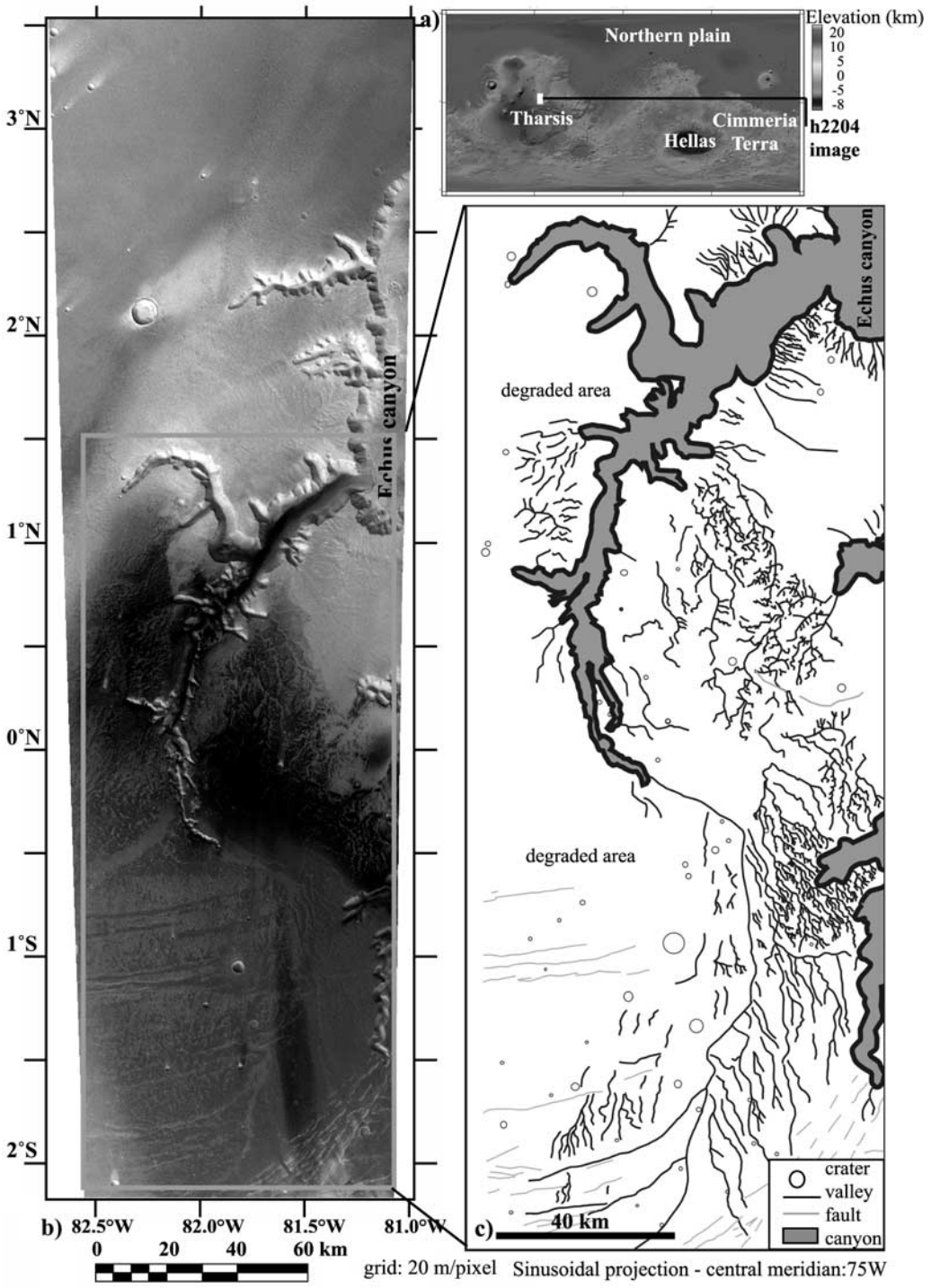

Figure 18. The western Echus plateau in a triplet of HRSC images (H2204). (a) Location of the HRSC images on a MOLA map, eastward of the Tharsis dome. (b) Subset of the HRSC H2204 nadir image at 20 m pixel^{-1}. The plateau west of Echus Chasma has a smooth surface to the north and dendritic valley networks incising dark material to the south. (c) Map of valley networks incising the Echus plateau made using classic photointerpretation methods.

controls their spatial resolution, the image quality (compression ratio, aerosols, etc.), and the surface roughness. If all of these parameters are good, then the spatial resolution of the HRSC DEMs is expected to be close to that of the stereo images. The surface roughness is a crucial parameter, because the stereogrammetry method is based on the recognition of homologous points. This method is very relevant when the surface is hilly and rough such as in the south Aeolis-Cimmeria highlands (Figures 2 and 3d). In such cases, we can favor the detection of topographic/

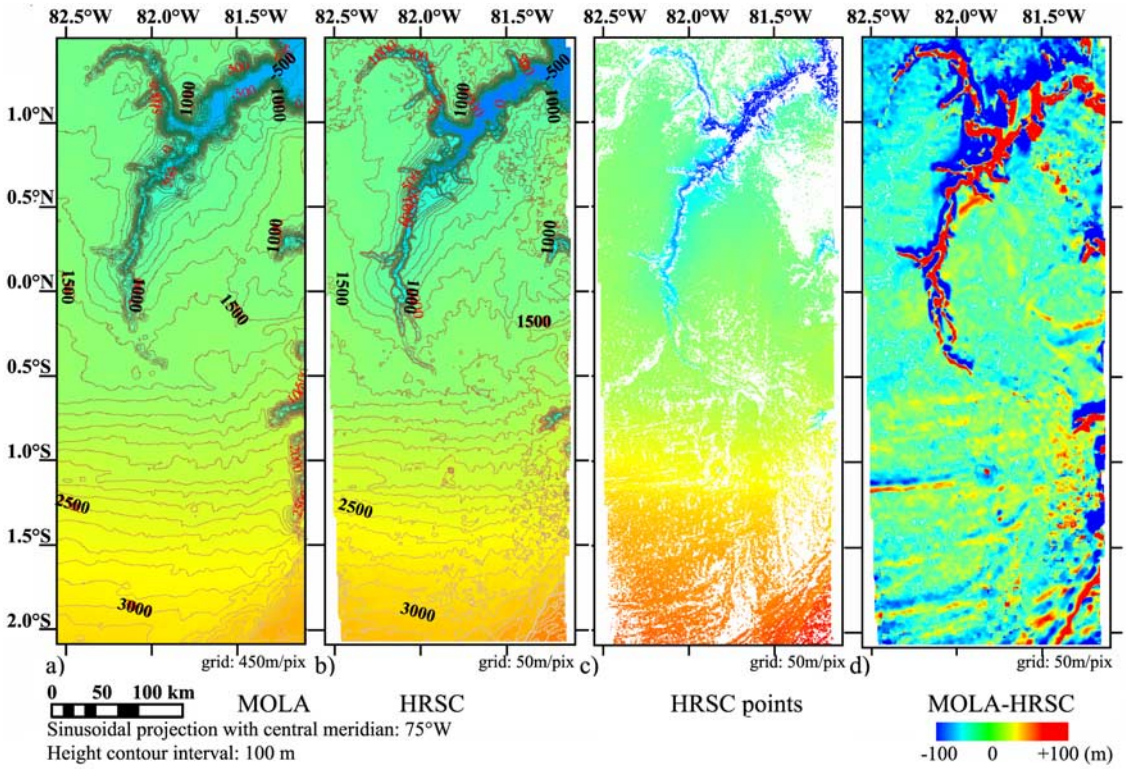

Figure 19. (a) MOLA topographic map of this area at 450 m pixel^{-1}. (b) The HRSC DEM generated from a population of 3-D object points distributed in a regular grid of 50 m pixel^{-1} seen in Figure 19c. Note that the part of the plateau where valley networks are found is well covered by 3-D object points. (d) The vertical offset between MOLA and the HRSC DEM is small.

geologic features and provide well-defined 3-D valleys geometry by adjusting the width of the spatial grid to that of the image spatial resolution (Figures 5 to 10).

[69] A negative aspect of this method is that it does not provide good topography when the surface is smooth. When the illumination and albedo are uniform, the distinction of different points on the smooth surface tends to zero: no 3-D object point can define the altitude. This is particularly true when dust mantles the area such as in the northern part of the Echus plateau (Figures 18 and 19c), or on smooth plains, such as a few crater floors near Huygens impact crater (Figures 11 and 12c). When we combine abundant smooth areas with heterogeneous image resolution, such as in the Huygens region, the number of detected points is low relative to the area covered by the images, and the scale of the spatial grid is degraded (at Huygens up to 250 m pixel^{-1}), preventing a detailed topographic analysis of the HRSC DEM compared to MOLA.

[70] Another limitation is the height offset that is observed between the two data sets, such as in the Huygens region (Figure 12d). In previous work using the HRSC DEMs, the height offset was found to be ~100 m [*Scholten et al.*, 2005, Table 1] or decreased to 25 m by improvement of exterior orientation data [*Heipke et al.*, 2006, 2007, *Spiegel et al.*, 2007; K. Gwinner et al., Derivation and validation of high-resolution digital terrain models from Mars Express HRSC-Data, submitted to *Photogrammetric Engineering and Remote Sensing*, 2007]. The offset is especially due to a lower constraint on the geometry of acquisition during the HRSC camera flights or less accurate exterior orientation data. These factors can be improved using a recently developed photogrammetry software program with bundle adjustment [*Heipke et al.*, 2007; *Spiegel et al.*, 2007]. The regional height offset is often low (<25 m) in the studied areas. We did not improve the processing here, as it would not affect the automatic detection of valleys.

[71] The statistical accuracy of elevation is usually <30 m, e.g., in the Aeolis and Huygens regions. This height accuracy is close to the pixel width in the input image, which is expected with the process of photogrammetry. This statistical height accuracy on each detected point is far from the height accuracy of ~1 m for MOLA. This latter value is valid over smooth surfaces, but the spatial grid of MOLA cannot account for such high vertical resolution on hilly terrains. As a consequence, a valuable strategy would be to combine the HRSC DEM in rough hilly regions with the MOLA shot topography over smooth plains and plateaus.

4.2. HRSC Improvements for Valley Network Geometry

[72] The automatic detection of valley networks has been greatly improved by the high spatial resolution of the HRSC DEMs compared to the MOLA grid. The automatic extraction is very efficient when the spatial grid size of the HRSC DEM is <100 m, e.g., in the south Aeolis region (Figure 4) and the central Echus plateau (Figure 18). Whatever the studied area, the number of drainage basins is always greater than the number found using MOLA (Table 1).

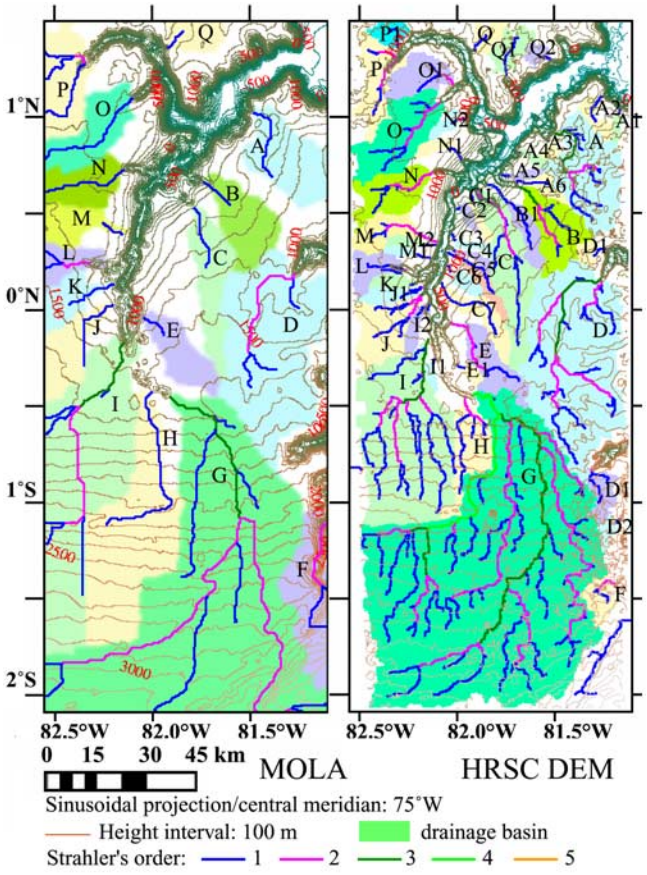

Figure 20. Comparative maps of valley networks detected automatically in MOLA and the HRSC DEMs, which have different spatial resolution. Drainage basins are bounded by their colored area and assigned a letter. Each Strahler order is identified by a color. In the HRSC DEM, more valley networks are detected with more tributaries than are found in MOLA. Each main tributary connects to the tributaries of the Echus canyon.

There is no systematic relationship between the number of drainage basins and the scale factor between MOLA and the HRSC DEM. The increase in drainage basins detected in the HRSC DEMs is due to a better spatial grid size, permitting a detailed definition of drainage basins. The consequence of this increase in the number of drainage basins is the decrease in individual drainage area (Table 1). The area covered by an HRSC image limits the automatic extraction of valley networks at local to regional scales. The main advantage of the HRSC DEMs is therefore the detailed study of small drainage basins of <100 km in width.

[73] The automatic detection provides a maximum Strahler order that is higher in the HRSC DEM than in MOLA (Table 1). The drainage density also increases significantly from MOLA to the HRSC DEM (Table 1), when it is calculated with the totality of basins recognized, or with drainage basins containing networks of Strahler order 3 or greater. For each studied region, we find with MOLA a maximum drainage density that is similar to that of other Martian regions, e.g., 0.06 to 0.25 km^{-1} [*Irwin and Howard*, 2002; *Stepinski and Collier*, 2003; *Stepinski and Stepinski*, 2005; *Luo and Stepinski*, 2006; *Ansan and Mangold*, 2006]. However, when we calculate the drainage density using the HRSC DEMs, it increases at least by a factor of 2, reaching 0.45 km^{-1} in the best spatial resolution of the HRSC DEMs analyzed in this study (Table 1). Despite this increase in drainage density in the HRSC DEMs, these values remain lower than the values in the manual mapping from the HRSC imagery. There is no systematic relationship between the drainage density in each data set and their scale. This is likely due to image quality and surface properties that inhibit the detection of the smallest valleys. In all data sets, the mean bifurcation ratio Rb and length ratio Rl follow the fractal empirical laws established for terrestrial fluvial valley networks [*Horton*, 1945]: the terrestrial bifurcation ratio Rb ranges from 3.0 to 5.0, and the terrestrial length ratio Rl ranges from 1.5 to 3.5 [*Horton*, 1945; *Ritter et al.*, 2002]. No major differences are observed between data sets, suggesting that the fractal properties of valleys limit any scattering of these values with different scales. This observation confirms that these two parameters are not useful in the understanding of fluvial processes.

4.3. HRSC Improvements for Geometry of Individual Valleys

[74] If we compare the geometry of individual valleys identified from gridded MOLA data and the HRSC DEMs, we see that the latter give better information on valley width and depth. Shallow and narrow valleys, typically <50 m in depth and <1 km in width, were resolved in the transverse profiles in the HRSC DEMs. This finding is especially true for valleys networks on the Echus plateau, where valleys as shallow as 20 m were detected (Figure 21). The HRSC DEMs are sometimes able to detect several smaller valleys where MOLA showed just one wide valley (e.g., Figure 9a). They also improve the resolution of the V shape or U shape of valleys that can be seen in imaging. The MOLA grid usually smoothed the relief at the 500-m scale, even if we used MOLA shot data spaced by 300 m along ground tracks, whereas the HRSC DEMs provide a section more consistent with the apparent shape on the visible image. In addition, in relatively few cases, the transverse topographic profiles extracted from the HRSC DEMs provide a better view of valley side slopes, with an increase by a factor of 2 compared to those extracted from MOLA gridded data (e.g., Figure 7a). These measurements are important for interpreting slope processes, which are major contributors to valley development, and the depth and cross-sectional profiles of valleys can provide important insights into their developmental history.

[75] The difference between the HRSC DEMs and the MOLA gridded data is less important for longitudinal profiles. In all studied areas, there is no significant difference between the longitudinal profiles of major tributaries extracted from the HRSC DEMs and MOLA. Some improvements come in resolving local features such as knickpoints. For example, in the Noachian terrain, the longitudinal profiles of major tributaries may be deformed by later wrinkle ridges (Figures 10, 14, 15, and 16). The HRSC scale can improve the understanding of these knickpoints, especially to determine whether valleys continued to form during or after the compressional faulting. The HRSC

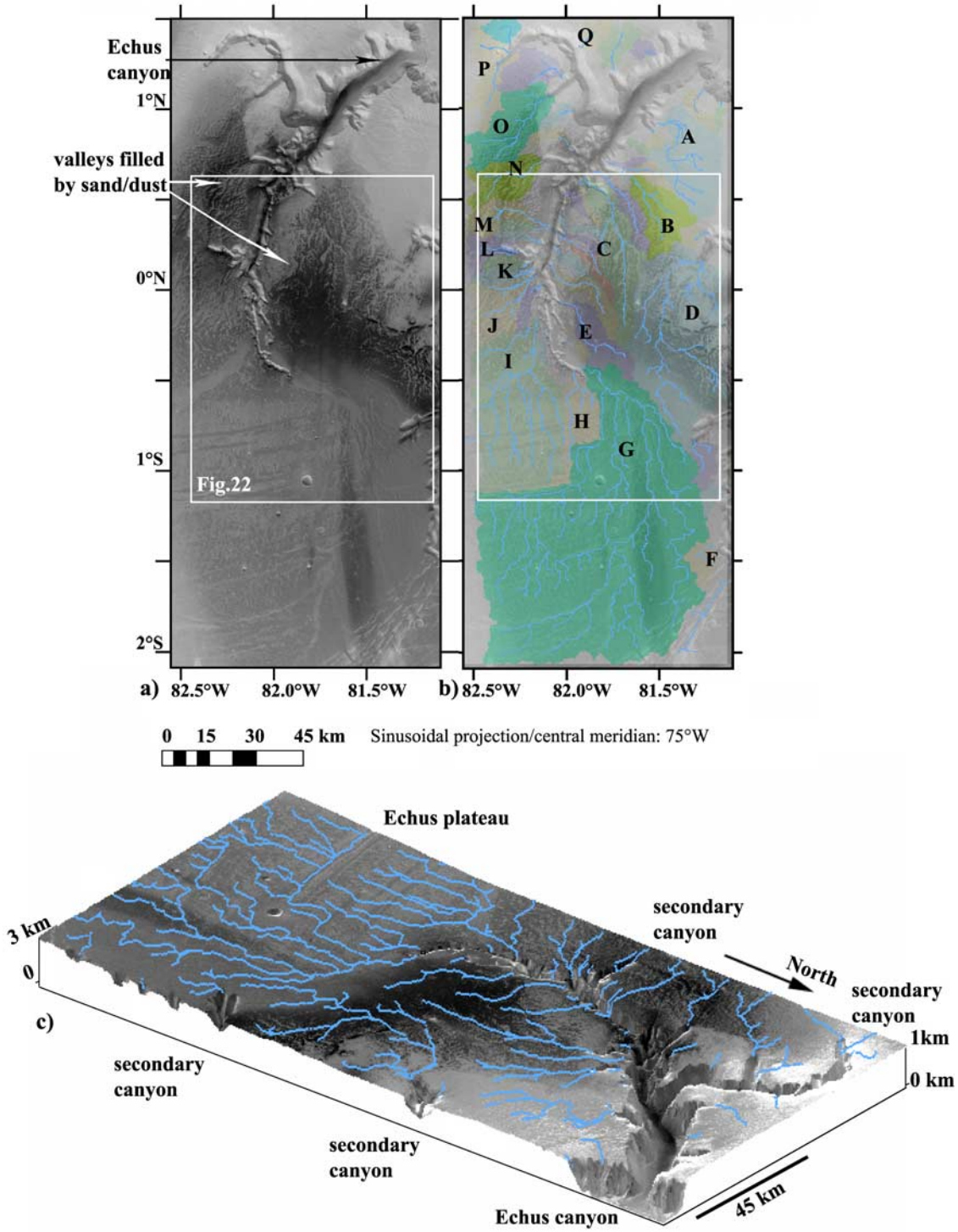

Figure 21. Detailed study of the Echus plateau. (a) H2204 nadir image (20 m pixel^{-1}). (b) Location of valley networks (blue lines) detected automatically in the HRSC DEM and their main associated drainage basins superimposed on the HRSC nadir image. (c) The 3-D view of the HRSC image with blue tributaries detected automatically in the HRSC DEM overlaid on the HRSC DEM. Note the change in pattern of valley networks with topographic slope (parallel orientation to the south and more dendritic to the north), and the connection between valley networks on plateau and the Echus canyon.

DEMs also enable us to extract longitudinal profiles of secondary valleys not detected by MOLA.

[76] In summary, the HRSC DEMs greatly improve the spatial resolution of the topography (down to 20 m pixel^{-1}) relative to MOLA gridded data ($\sim$500 m pixel^{-1}), essentially when the triplet of images has good spatial resolution ($\leq$50 m pixel^{-1}), sufficient albedo contrast, and high surface roughness. A main problem with the HRSC DEMs

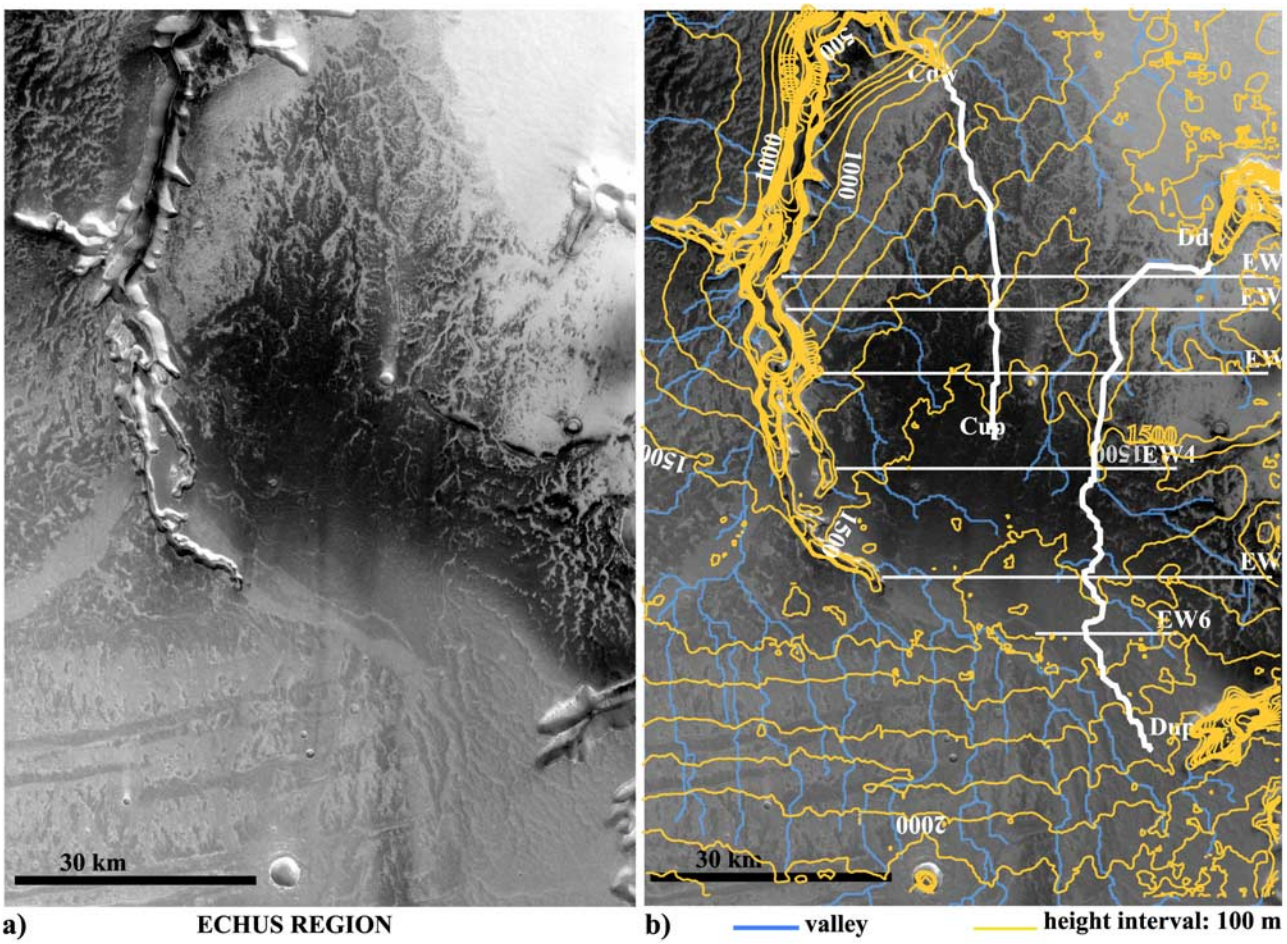

Figure 22. Detailed study of the central part of the Echus plateau (Figure 21). (a) Detail of the H2204 nadir image (20 m pixel^{-1}). (b) Location of valley networks (blue lines) detected automatically in the HRSC DEM superimposed on the HRSC nadir image. The thick white lines correspond to the locations of longitudinal topographic profiles plotted in Figure 23. The E-W trending thin white lines correspond to the locations of transverse profiles (Figure 23). Yellow contour lines are spaced at 100-m intervals.

comes from the lack of matching points in the smooth regions, but this limitation does not account for most valley networks, whose relief is rough by nature. The automatic extraction of valleys between the two data sets at the same level of detection (cells of accumulation flow multiplied by the scale ratio between the MOLA and the HRSC DEMs) shows a strong improvement in the pattern and drainage density (by a factor of 2 to 4). Drainage densities become close to those mapped manually when the HRSC DEM parameters are optimal. A fundamental improvement comes in the transverse profiles of individual valleys, which give precise depths and shape. Longitudinal profiles are sometimes more accurate, especially for smaller valleys, and they resolve knickpoints and other irregularities more effectively.

5. Discussion 2: Implications for the Formation Processes of Valley Networks

5.1. Process of Erosion and Surface-Subsurface Interactions

[77] We have studied three distinct regions containing valley networks of different ages. In each studied region, whatever the data set used (MOLA, the HRSC DEMs and images), we find that valley networks are arranged in subcircular to elongated drainage basins with dendritic or subparallel patterns, showing the same morphometric characteristics as are found in terrestrial fluvial valley networks: (1) valley heads are usually distributed along the watershed boundary at different elevations, (2) valleys have either V shapes or occasionally trapezoidal shapes, (3) valley widths increases downstream, (4) longitudinal profiles are linear to concave, and (5) valleys are arranged in branching patterns controlled by the topographic slope. These observations support the idea that the Martian valleys formed in a climate in which rainfall and/or snowfall and where subsequent snowmelt induced overland flow [*Craddock and Howard*, 2002; *Mangold et al.*, 2004a, 2004b; *Howard et al.*, 2005; *Irwin et al.*, 2005b; *Ansan and Mangold*, 2006].

[78] On Earth, these processes supply a groundwater table that allows water to seep. What observations would suggest the occurrence of a water cycle with subsurface infiltration and recharge of aquifers? Examples in the surroundings of Huygens impact crater and the Echus plateau suggest a coeval formation of valleys by runoff and by seepage. In the surroundings of Huygens crater, the divide between the two

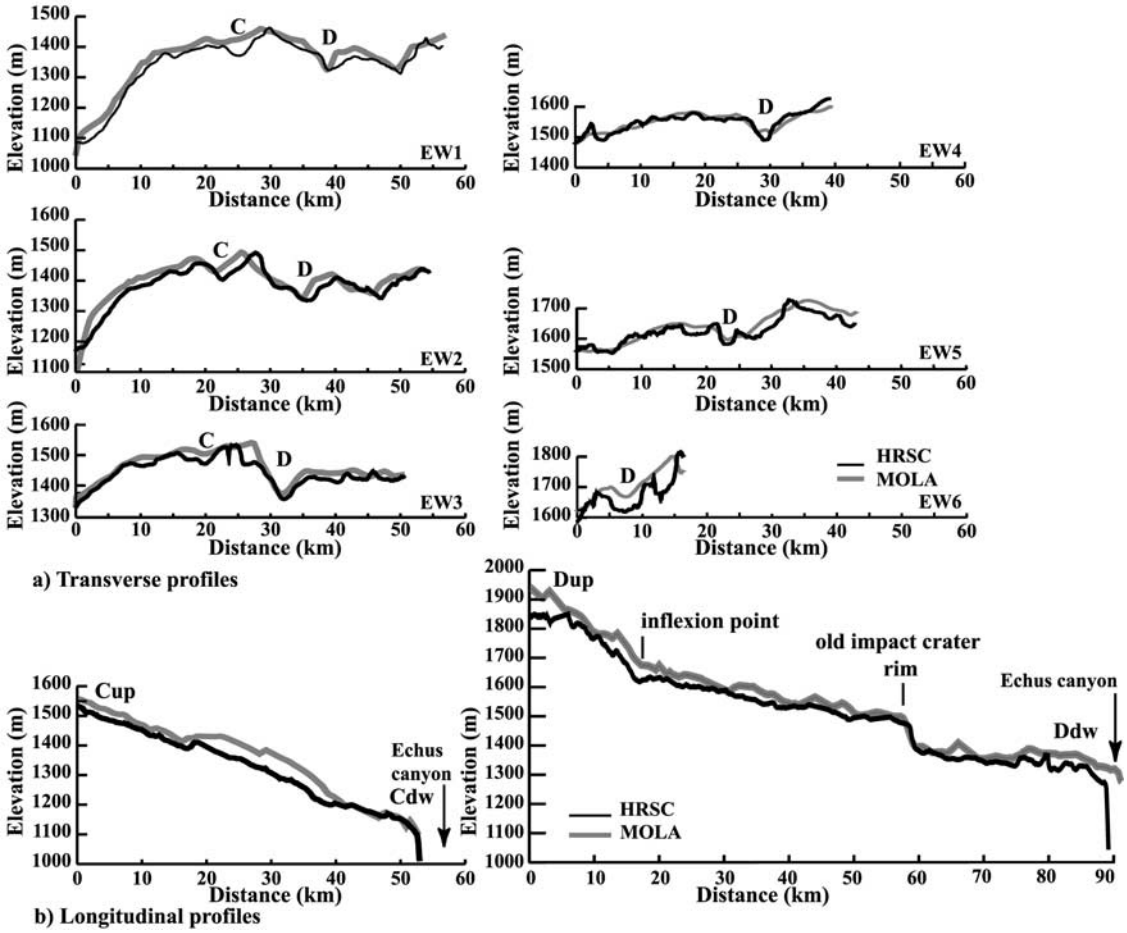

Figure 23. (a) Transverse topographic profiles across the Echus plateau. See their location in Figure 22. The major valleys are 80 m deep, whereas the smallest ones have a depth of 20 m. (b) Longitudinal profiles along tributaries C and D on the Echus plateau, with locations shown in Figure 22. The profiles have a straight shape parallel to the regional topographic slope. See the topographic jump in profile Dup-Ddw due to the old impact crater rim. The depth of the Echus canyon is 400 m.

opposite-facing drainage basins P and Q (Figure 16) stands at 2200 m in elevation. The sharpness of this divide and lack of an upslope aquifer has been interpreted as evidence of atmospheric recharge and overland flows [*Irwin et al.*, 2005a, 2005b]. However, the longitudinal profiles (Figure 17b) suggest that back-wasting erosion occurred in order to connect the two drainage basins. The divide is 500 m lower than valley heads located on the Huygens crater rim southward (Figure 16b), suggesting that a possible groundwater table stood at 2200 m in elevation during the last hydrologic discharge event.

[79] On the Echus plateau, the competition between runoff and sapping processes is well expressed. Shallow valley networks that developed on the plateau invoke a dominant runoff process. When the depth of valleys is sufficient to reach the base of volcanic impermeable and easily eroded materials, water infiltrated and recharged the groundwater table. At places where groundwater table crossed the topography, the sapping process could occur, forming the amphitheater-shaped valley heads of the Echus tributary canyons (see *Mangold et al.* [2008] for details).

5.2. Implications of Drainage Density

[80] The Martian valley networks studied from the HRSC images have relatively well developed headward extension with up to fifth-order network in Strahler's system, and manual mapping indicates relatively high drainage densities up to 1 km^{-1}. This drainage density increases from the Huygens region to the south Aeolis region and the Echus plateau, with a respective maximum drainage density of 0.3, 0.5, and 0.8 km^{-1} (Table 1). However, this increase in drainage density is not correlated with an increase in valley depth. Main valleys are up to 400 m deep in the Huygens region, and those in the Aeolis region reach only 200 m of depth, whereas the major valleys never exceed 80 m deep on the Echus plateau.

[81] The lack of a systematic relationship between drainage density and the depth of major tributaries may be due to differences in various parameters such as lithology, erosive processes (advective fluvial incision, diffusive mass wasting), or timescale of incision. The problem is that the drainage density does not record the duration or efficiency of the process beyond an initial period of network devel-

opment. The number of valleys and drainage density increase up to a maximum extension, and then the network stops growing when the contributing area is completely incised. In shallowly incised drainage networks, drainage density may primarily reflect the combination of contributing area and topographic slope that are necessary to initiate incision [*Montgomery and Dietrich*, 1988]. By comparison, competition between diffusive mass wasting and advective fluvial incision determines drainage density in more deeply incised networks with well-developed side slopes.

[82] The lower drainage density of Noachian terrains can also be explained by the history of degradation through impact cratering and aeolian processes, which modified the shallower tributaries of older valley networks more significantly than younger ones. The highest drainage densities on Mars were found for the youngest valleys, such as 1 km^{-1} on the Echus plateau [*Mangold et al.*, 2008, this study], 1.5 km^{-1} on Alba Patera and 2.3 km^{-1} on Hecates Tholus [*Gulick and Baker*, 1990]. This trend might represent a better preservation of the smallest tributaries due to their younger age rather than a more mature development of these networks. In summary, drainage density does not represent a degree of erosion of the valley systems after a significant extension in 2-D is reached, and these examples suggest that it should not be used as an unique indicator of valley development.

5.3. Valley Evolution with Time

[83] How long did it take for these valleys to form? Timescales are difficult to estimate using crater counting. These methods can constrain the absolute age of the surface carved by the valley networks and the determination of activity, but not the duration of incision (e.g., Warrego Valles [*Ansan and Mangold*, 2006]). Terrestrial valley networks in different climatic and lithologic contexts (volcanic plains or glacial till) usually form over timescales from 10,000 years to 1 Ma [*Knox*, 1976; *Pizzuto*, 1992; *Knighton*, 1998]. From our results, we can discuss the duration based on the total incision and the longitudinal profiles. Brief fluvial incision of a weak material or more prolonged incision of a strong material can result in similar morphometric properties. The shallow valleys on the Echus plateau formed in a weak upper layer deposited on the basement, and they have fully incised and extended throughout the drainage basin [see *Mangold et al.*, 2008]. These observations suggest that the well-developed valleys in the Echus region result from a quicker erosive activity in weaker material, such as shallow fluvial landforms in terrestrial badlands or ash deposits. In contrast, the fluvial networks present in the Noachian terrain have a lower drainage density but deeper valleys. If we assume that Noachian terrain consists of a mixture of volcanic rocks, fragmented regolith from impact gardening, and clays resulting from their chemical alteration, then incision occurred over a longer period of time than on the Echus plateau in order to carve valleys that are 200 m deep.

[84] Longitudinal profiles also provide some clues for the duration of the processes. The more than 100-km-long longitudinal profiles often have a concave-up shape (Figures 5, 7, 10, 15, and 17), but this shape is observed in a limited number of networks, and profiles are often close to the regional topographic slope. This observation was also made in different regions of Mars using MOLA data [*Aharonson et al.*, 2002; *Irwin and Howard*, 2002; *Irwin et al.*, 2004; *Howard et al.*, 2005; *Ansan and Mangold*, 2006]. Nevertheless, compared to the Echus Chasma system where profiles are very straight, the profiles of Noachian age valleys are more concave and imply a longer evolution. This observation supports our conclusions based on the depth of valleys. The Echus plateau has shallower valleys in weaker material, suggesting lower incision and a shorter timescale of erosion. However, we cannot yet estimate an absolute duration of any valley system. This is a crucial objective for future studies, in order to know if Martian valley networks result from either episodic wet intervals not representative of the early Martian climate, or a long-term climate of more frequent, low-intensity events.

6. Conclusion

[85] HRSC DEMs were made using three stereoscopic images ranging from 10 to 100 m $pixel^{-1}$ resolution. The HRSC DEMs better represent the Martian topography at the regional scale compared to MOLA, thanks to their spatial grid sampling from 20 to 100 m $pixel^{-1}$. This spatial coverage in the HRSC DEMs permits the detection of small drainage basins ($\sim$100 km^2) in which valleys developed. The HRSC DEMs improve the quantification of valley network properties such as drainage density and aspect ratio compared to the MOLA DEM. These new data also confirm that the manual mapping of valleys with previous Viking or THEMIS images were justified in the studied regions; i.e., mapped valleys correspond to a true topographic signature. The other strength of the HRSC DEMs is the extraction of a higher number of shallower (<50 m deep) and narrower (<1 km wide) valleys than are found in MOLA. The topographic profiles across valleys are more accurate, improving our understanding of their transverse profiles, their downstream variation in width, and their longitudinal profiles.

[86] The three studied regions enable us to compare Noachian (Huygens and south Aeolis areas) and Hesperian age (Echus plateau) terrains. The comparison shows that the Hesperian valleys on the West Echus plateau are much shallower than are older valleys in Noachian terrain, despite the fact that their drainage density is higher. This difference probably arises for one or more of three possible reasons: (1) Noachian landforms are not as well preserved as are later episodes of fluvial activity, creating a difference in the identification of small tributaries, (2) the duration of Noachian fluvial activity might have been longer to explain the deeper incision of valleys and the removal of the smallest tributaries by this incision, and (3) the bedrock composition is likely different, explaining the development of more small tributaries in the weak upper unit of the Echus plateau than in Noachian terrains. This lack of correlation between drainage density and incision therefore shows the limitation on the use of 2-D parameters: the larger drainage density might not mean a longer period of valley formation, but a better preservation of the smallest tributaries. In addition, longitudinal profiles are concave only for well-developed valleys in the Noachian regions, suggesting that equilibrium was reached for these valleys. Such studies will be continued over larger areas to improve statistics in regions of

different ages and our understanding of Martian valley networks.

[87] **Acknowledgments.** We acknowledge the effort of the HRSC Co-Investigator Team members and their associates who have contributed to this investigation in the preparatory phase and in scientific discussions within the teams. We thank F. Scholten and R. Schmidt for their technical help and advice, in using DLR's photogrammetry software. We thank R. Irwin and the anonymous reviewer for their detailed reviews on valley networks. We are grateful for the W. Hartmann's and R. Irwin's help regarding English usage in several parts of this paper. French authors were supported by the Programme National de Planétologie (PNP) of the Institut National des Sciences de l'Univers (INSU) and the Centre National d'Etude Spatial (CNES).

References

Aharonson, O., M. T. Zuber, D. H. Rothman, N. Schorghofer, and K. X. Whipple (2002), Drainage basins and channel incision on Mars, *Proc. Natl. Acad. Sci. U.S.A.*, *99*(4), 1780–1783, doi:10.1073/pnas.261704198.

Albee, A. L., F. D. Palluconi, and R. E. Arvidson (1998), Mars Global Surveyor mission: Overview and status, *Science*, *279*, 1671–1672, doi:10.1126/science.279.5357.1671.

Albertz, J., et al. (2005), HRSC on Mars Express-Photogrammetric and cartographic research, *Photogramm. Eng. Remote Sens.*, *71*(10), 1153–1166.

Ansan, V., and N. Mangold (2006), New observations of Warrego Valles. Mars: Evidence for precipitation and surface runoff, *Planet. Space Sci.*, *54*, 219–242, doi:10.1016/j.pss.2005.12.009.

Ansan, V., N. Mangold, P. Masson, C. Quantin, G. Neukum, and HRSC team (2005), Quantifying valley network parameters on Mars using DEM from HRSC/MEX data, *Eos Trans. AGU*, *86*(52), Fall Meet. Suppl., Abstract P21B-0146.

Ansan, V., N. Mangold, P. Masson, G. Neukum, and the HRSC Co-Investigator Team (2007a), Analysis of Noachian valley networks in Aeolis region, Mars, from HRSC/MEX images and DTM, *Geophys. Res. Abstr.*, *9*, 09722.

Ansan, V., N. Mangold, P. Masson, G. Neukum, and the HRSC Co-Investigator Team (2007b), Topography of valley networks on Mars: Comparison between MOLA and HRSC DTM, *Lunar Planet. Sci. Conf.*, *XXXVIII*, Abstract 1660.

Baker, V. R. (1982), *The Channels of Mars*, 198 pp., Univ. of Tex. Press, Austin.

Baker, V. R. (1985), Models of fluvial activity on Mars, in *Models in Geomorphology*, edited by M. Woldenberg et al., pp. 287–312, Allen and Unwin, Boston, Mass.

Baker, V. R. (1990), Spring sapping and valley network development, in *Groundwater Geomorphology: The Role of Subsurface Water in Earth-Surface Processes and Landform*, edited by C. G. Higgins and D. R. Coates, *Spec. Pap. Geol. Soc. Am. Bull*, 252, 235–265.

Baker, V. R., and J. Partridge (1986), Small Martian valleys: pristine and degraded morphology, *J. Geophys. Res.*, *91*, 3561–3572, doi:10.1029/JB091iB03p03561.

Baker, V. R., M. H. Carr, V. C. Gulick, C. R.Williams, and M. S. Marley (1992), Channels and valley networks, in *Mars*, edited by H. H. Kieffer et al., pp. 493–522, Univ. of Ariz. Press, Tucson.

Brakenridge, G. R. (1990), The origin of fluvial valleys and early geologic history: Aeolis quadrangle, Mars, *J. Geophys. Res.*, *95*, 17,289–17,308, doi:10.1029/JB095iB11p17289.

Cabrol, N. A., and E. A. Grin (2001), Composition of the drainage network on early Mars, *Geomorphology*, *37*, 269–287, doi:10.1016/S0169-555X(00)00087-8.

Carr, M. H. (1981), Mars, in *The Geology of Terrestrial Planets*, edited by M. H. Carr, NASA Spec. Publ., *SP-469*, 207–263.

Carr, M. H. (Ed.) (1996), *Water on Mars*, 229 pp., Oxford Univ. Press, New York.

Carr, M. H., and F. C. Chuang (1997), Martian drainage densities, *J. Geophys. Res.*, *102*, 9145–9152, doi:10.1029/97JE00113.

Carr, M. H., and G. D. Clow (1981), Martian channels and valleys: Their characteristics, distribution, and age, *Icarus*, *48*, 91–117, doi:10.1016/0019-1035(81)90156-1.

Carr, M. H., and M. C. Malin (2000), Meter-scale characteristics of Martian channels and valleys, *Icarus*, *146*, 366–386, doi:10.1006/icar.2000.6428.

Chicarro, A., P. Martin, and R. Trautner (2004), The Mars Express Mission: An overview, *Eur. Space Agency Spec. Publ.*, *SP-1240*, 3–16.

Christensen, P. R., et al. (2003), Morphology and composition of the surface of Mars: Mars Odyssey THEMIS results, *Science*, *300*, 2056–2061, doi:10.1126/science.1080885.

Craddock, R. A., and A. D. Howard (2002), The case for rainfall on a warm, wet early Mars, *J. Geophys. Res.*, *107*(E11), 5111, doi:10.1029/2001JE001505.

De Hon, R. A. (1978), Geologic map of the Eridania quadrangle of Mars (MC-29), scale 1:5,000,000, *U.S. Geol. Surv. Map*, *I-1008*.

Dohm, J. M., and K. L. Tanaka (1999), Geology of Thaumasia region Mars: Plateau development valley origins and magmatic evolution, *Planet. Space Sci.*, *47*, 411–431, doi:10.1016/S0032-0633(98)00141-X.

Duxbury, T. C., R. L. Kirk, B. A. Archinal, and G. A. Neumann (2002), Mars geodesy/cartography working group recommendation on Mars cartographic constants and coordinate systems, paper presented at Joint International Symposium on Geospatial Theory, Processing and Application, Int. Soc. for Photogramm. and Remote Sens., Ottawa, Ont.

Goldspiel, J. M., and S. W. Squyres (2000), Groundwater sapping and valley formation on Mars, *Icarus*, *148*, 176–192, doi:10.1006/icar.2000.6465.

Goldspiel, J. M., S. W. Squyres, and D. G. Jakowski (1993), Topography of small Martian valleys, *Icarus*, *105*, 479–500, doi:10.1006/icar.1993.1143.

Grant, J. A. (2000), Valley formation in Margaritifer Sinus, Mars, by precipitation-recharged ground-water sapping, *Geology*, *28*, 223–226, doi:10.1130/0091-7613(2000)28<223:VFIMSM>2.0.CO;2.

Greeley, R., and J. J. Guest (1987), Geologic map of the eastern equatorial region of Mars, scale 1:15,000,000, *U.S. Geol. Surv. Map*, *I-1802-B*.

Gulick, V. C. (1998), Magmatic intrusions and hydrothermal origin for fluvial valleys on Mars, *J. Geophys. Res.*, *103*, 19,365–19,387, doi:10.1029/98JE01321.

Gulick, V. C. (2001), Origin of the valley networks on Mars: A hydrological perspective, *Geomorphology*, *37*, 241–268, doi:10.1016/S0169-555X(00)00086-6.

Gulick, V. C., and V. R. Baker (1989), Fluvial valleys and Martian paleoclimates, *Nature*, *341*, 514–516, doi:10.1038/341514a0.

Gulick, V. C., and V. R. Baker (1990), Origin and evolution of valleys on Martian volcanoes, *J. Geophys. Res.*, *95*, 14,325–14,344, doi:10.1029/JB095iB09p14325.

Gwinner, K., F. Scholten, R. Jaumann, T. Roatsch, J. Oberst, and G. Neukum (2007), Global mapping of Mars by systematic derivation of Mars Express HRSC high-resolution digital elevation models and orthoimages, paper presented at Extraterrestrial Mapping Workshop on Advances in Planetary Mapping 2007, ISPRS Comm. IV, Working Group 9, Houston, Tex.

Hartmann, W. K. (2005), Martian cratering: 8. Isochron refinement and the history of Martian geologic activity, *Icarus*, *174*, 294–320, doi:10.1016/j.icarus.2004.11.023.

Hartmann, W. K., and G. Neukum (2001), Cratering chronology and the evolution of Mars, *Space Sci. Rev.*, *96*, 165–194, doi:10.1023/A:1011945222010.

Heipke, C., et al. (2006), The HRSC DTM test, Int, *Arch. Photogramm. Remote Sens. Spatial Inf. Sci.*, *36*(4), 311–325.

Heipke, C. et al. (2007), Evaluating planetary digital terrain models-The HRSC DTM Test, paper presented at Extraterrestrial Mapping Workshop on Advances in Planetary Mapping 2007, ISPRS Comm. IV, Working Group 9, Houston, Tex.

Horton, R. E. (1945), Erosional development of streams and their drainage basin: Hydrophysical approach to quantitative morphometry, *Geol. Soc. Am. Bull.*, *56*, 275–370, doi:10.1130/0016-7606(1945)56[275:EDOSAT]2.0.CO;2.

Howard, A. D., , R. C. Kochel, and H. E. Holt (Eds.) (1988), *Sapping Features of the Colorado Plateau: A Comparative Planetary Geology Field Guide*, NASA Spec. Publ., *SP-491*, 108 pp.

Howard, A. D., J. M. Moore, and R. P. Irwin (2005), An intense terminal epoch of widespread fluvial activity on early Mars: 1. Valley network incision and associated deposits, *J. Geophys. Res.*, *110*, E12S14, doi:10.1029/2005JE002459.

Irwin, R. P., and A. D. Howard (2002), Drainage basin evolution in Noachian Terra Cimmeria, Mars, *J. Geophys. Res.*, *107*(E7), 5056, doi:10.1029/2001JE001818.

Irwin, R. P., A. D. Howard, and T. A. Maxwell (2004), Geomorphology of Ma'adim Vallis, Mars, and associated paleolake basins, *J. Geophys. Res.*, *109*, E12009, doi:10.1029/2004JE002287.

Irwin, R. P., R. A. Craddock, and A. D. Howard (2005a), Interior channels in Martian valley networks: Discharge and runoff production, *Geology*, *33*(6), 489–492, doi:10.1130/G21333.1.

Irwin, R. P., A. D. Howard, R. A. Craddock, and J. M. Moore (2005b), An intense terminal epoch of widespread fluvial activity on early Mars: 2. Increased runoff and paleolake development, *J. Geophys. Res.*, *110*, E12S15, doi:10.1029/2005JE002460.

Jaumann, R., et al. (2005), Interior channels in Martian valleys: Constraints on fluvial erosion by measurements of the Mars Express High Resolution Stereo Camera, *Geophys. Res. Lett.*, *32*, L16203, doi:10.1029/2005GL023415.

Jaumann, R., et al. (2007), The high resolution stereo camera (HRSC) experiment on Mars express: Instrument aspects and experiment conduct from interplanetary cruise through the nominal mission, *Planet. Space Sci.*, *55*, 928–952, doi:10.1016/j.pss.2006.12.003.

Knighton, D. (1998), *Fluvial Forms and Processes: A New Perspective*, 383 pp., Oxford Univ. Press, New York.

Knox, J. C. (1976), Concept of the graded stream, in *Theories of Landform Development*, edited by W. Melhom and R. Flemal, pp. 168–198, Allen and Unwin, London.

Loesch, T. N. (2001), Hydrologic analysis using GIS, paper presented at Spring Workshop, Minn. GIS/LIS Consort., Alexandria, Minn.

Luo, W., and T. F. Stepinski (2006), Topographycally derived maps of valley networks and drainage density in the mare Tyrrhenum quadrangle of Mars, *Geophys. Res. Lett.*, *33*, L18202, doi:10.1029/2006GL027346.

Malin, M. C., and M. H. Carr (1999), Groundwater formation of Martian valleys, *Nature*, *397*, 589–591, doi:10.1038/17551.

Malin, M. C., and K. S. Edgett (2000), Evidence for recent groundwater seepage and surface runoff on Mars, *Science*, *288*, 2330–2335.

Malin, M. C., et al. (1998), Early views of the Martian surface from the Mars Orbiter Camera of Mars Global Surveyor, *Science*, *279*, 1681–1685, doi:10.1126/science.279.5357.1681.

Mangold, N., C. Quantin, V. Ansan, C. Delacourt, and P. Allemand (2004a), Evidence for precipitation on Mars from dendritic valleys in the Valles Marineris area, *Science*, *305*, 78–81, doi:10.1126/science.1097549.

Mangold, N., C. Quantin, V. Ansan, C. Delacourt, P. Paillou, and P. Allemand (2004b), Dendritic valley networks of Hesperian age on Valles Marineris plateau, paper presented at Workshop on Mars Valley Networks, Smithson. Inst., Kohala Coast, Hawaii.

Mangold, N., V. Ansan, P. Masson, C. Quantin, G. Neukum, and HRSC Co-Investigator Team (2005a), Late episodes of fluvial valleys formation on Mars from HRSC/MEX data, *Eos Trans. AGU*, *86*(52), Fall Meet. Suppl., Abstract H31G-04.

Mangold, N., P. Masson, V. Ansan, C. Quantin, G. Neukum, and HRSC Co-I Team (2005b), Analysis of valley networks on Valles Marineris plateau using HRSC/MEX data, *Lunar Planet. Sci. Conf.*, *XXXV*, Abstract 1336.

Mangold, N., V. Ansan, P. Masson, C. Quantin, G. Neukum, and HRSC co-Investigator Team (2007), Analysis of West Echus Chasma valleys, Mars, from HRSC/MEX images and DTM, *Geophys. Res. Abstr.*, *9*, 09657.

Mangold, N., V. Ansan, P. Masson, C. Quantin, and G. Neukum (2008), Geomorphic study of fluvial landforms on the northern Valles Marineris plateau, Mars, *J. Geophys. Res.*, doi:10.1029/2007JE002985, in press.

Mars Channel Working Group (1983), Channels and valleys on Mars, *Geol. Soc. Am. Bull.*, *94*, 1035–1054, doi:10.1130/0016-7606(1983)94<1035:CAVOM>2.0.CO;2.

Masson, P., V. Ansan, J. Lanz, N. Mangold, C. Quantin, E. Hauber, R. Jaumann, and G. Neukeum (2004), New observations of valley networks using THEMIS (MARS odyssey) and HRSC data (MARS EXPRESS), paper presented at Early Mars Conference, Lunar and Planet. Inst., Jackson Hole, Wyo.

Masson, P., V. Ansan, N. Mangold, C. Quantin, G. Neukum, and HRSC Co-I Team (2005), HRSC/MEX analysis of valley networks on Echus Chasma Plateau and in Aeolis region, *Lunar Planet. Sci. Conf.*, *XXXVI*, Abstract 1340.

Milton, D. J. (1973), Water and processes of degradation in the Martian landscape, *J. Geophys. Res.*, *78*, 4037–4047, doi:10.1029/JB078i020p04037.

Montgomery, D. R., and W. E. Dietrich (1988), Where do channels begin?, *Nature*, *336*, 232–234, doi:10.1038/336232a0.

Neukum, G., R. Jaumann, and the HRSC Co-Investigator Team (2004), HRSC: The high resolution stereo camera of Mars Express, *Eur. Space Agency Spec. Publ. ESA*, *SP-1240*, 17–36.

Neuman, G. A., F. G. Lemoine, D. E. Smith, and M. T. Zuber (2003), The Mars Orbiter Laser Altimeter archive: Final precision experiment data record release and status radiometry, *Lunar Planet. Sci. Conf.*, *XXXIV*, Abstract XXXX.

Pieri, D. C. (1980), Martian valleys: Morphology, distribution, age and origin, *Science*, *210*, 895–897, doi:10.1126/science.210.4472.895.

Pizzuto, J. E. (1992), The geomorphology of graded gravel rivers: A network perspective, *Geomorphology*, *5*, 457–474, doi:10.1016/0169-555X(92)90018-J.

Ritter, D. L., R. C. Kochel, and J. R. Miller (Eds.) (2002), *Process Geomorphology*, 560 pp., McGraw-Hill, Boston, Mass.

Schaber, G. G. (20051977), Geologic map of the Iapygia quadrangle of Mars 5MC-21), scale 1:5,000,000, *U.S. Geol. Surv. Map*, *I-1020*.

Scholten, F., K. Gwinner, T. Roasch, K.-D. Matz, M. Wählisch, B. Giese, J. Oberst, R. Jaumann, G. Neukum, and the HRSC Co-Investigator Team (2005), Mars express HRSC data processing, *Photogramm. Eng. Remote Sens.*, *71*(10), 1143–1152.

Schultz, P. H., and F. E. Ingerson (1973), Martian lineaments from Mariner 6 and 7 images, *J. Geophys. Res.*, *78*, 8415–8427, doi:10.1029/JB078i035p08415.

Schumm, S. A. (1956), Evolution of drainage systems and slopes in badlands at Perth Ambo, New Jersey, *Geol. Soc. Am. Bull.*, *67*, 597–646, doi:10.1130/0016-7606 (1956)67[597:EODSAS]2.0.CO;2.

Scott, H. S., and M. H. Carr (1978), Atlas of Mars: Geologic series (M 25MG), 1:25,000,000, *U.S. Geol. Surv. Map*, *I-1083*.

Scott, H. S., E. C. Morris, and M. N. Marretta (1978), Geologic map of the Aeolis quadrangle of Mars (MC-23), scale 1:5,000,000, *U.S. Geol. Surv. Map*, *I-1111*.

Scott, H. S., K. L. Tanaka, R. Greeley, and J. E. Guest (1986), Geologic maps of the western equatorial. eastern equatorial and polar regions of Mars, scale 1:15,000,000, *U.S. Geol. Surv. Map*, *I-1802-A, B and C*.

Seidelmann, P. K., V. K. Abablakin, M. Bursa, M. E. Davies, C. De Bergh, J. H. Leiske, J. Oberst, J. L. Simon, E. M. Standish, P. Stooke, and P. C. Thomas (2002), Report of the IAU/IAG working group on cartographic coordinates and rotational elements of the planets and satellites: 2000, *Celestial Mech. Dyn. Astron.*, *82*, 83–110, doi:10.1023/A:1013939327465.

Sharp, R. P., and M. C. Malin (1975), Channels on Mars, *Geol. Soc. Am. Bull.*, *86*, 593–609, doi:10.1130/0016-7606(1975)86<593:COM>2.0.CO;2.

Smith, D. E. (1998), Topography of the northern hemisphere of Mars from the Mars Orbiter Laser Altimeter, *Science*, *279*, 1686–1692, doi:10.1126/science.279.5357.1686.

Smith, D. E. (1999), The gravity field of Mars: results from Mars Global Surveyor, *Science*, *286*, 94–97, doi:10.1126/science.286.5437.94.

Smith, D. E., et al. (1999), The global topography of Mars and implications for surface evolution, *Science*, *284*, 1495–1503, doi:10.1126/science.284.5419.1495.

Spiegel, M., R. Schmidt, U. Stilla, and G. Neukum (2007), Improvement of exterior orientation of Mars Express HRSC imagery using a photogrammetric block, *Lunar Planet. Sci. Conf.*, *XXXVII*, Abstract 1608.

Squyres, S. W. (1989), Urey Price lecture: Water on Mars, *Icarus*, *79*, 229–288, doi:10.1016/0019-1035(89)90078-X.

Stepinski, T. F., and M. L. Collier (2003), Drainage densities of computationally extracted Martian drainage basins, paper presented at 6th International Conference on Mars, Lunar and Planet. Inst., Pasadena, Calif.

Stepinski, T. F., and A. P. Stepinski (2005), Morphology of drainage basins as an indicator of climate on early Mars, *J. Geophys. Res.*, *110*, E12S12, doi:10.1029/2005JE002448.

Strahler, A. N. (1952), Dynamic basis of geomorphology, *Geol. Soc. Am. Bull.*, *63*, 923–938, doi:10.1130/0016-7606(1952)63[923:DBOG]2.0.CO;2.

Tanaka, K. L. (1986), The stratigraphy of Mars, *Proc. Lunar Planet. Sci. Conf. 17th, Part 1*, *J. Geophys. Res.*, *91*, E139–E158, doi:10.1029/JB091iB13p0E139.

Tanaka, K. L., D. H. Scott, and R. Greeley (1992), Global stratigraphy, in *Mars*, edited by H. H. Kieffer et al., pp. 345–382, Univ. of Ariz. Press, Tucson.

Tanaka, K. L., J. M. Dohm, J. H. Lias, and T. M. Hare (1998), Erosional valleys in the Thaumasia region of Mars: Hydrothermal and seismic origin, *J. Geophys. Res.*, *103*, 31,407–31,420, doi:10.1029/98JE01599.

Watters, T. R. (1993), Compressional tectonism on Mars, *J. Geophys. Res.*, *98*, 17,049–17,060, doi:10.1029/93JE01138.

Wewel, F., F. Scholten, and K. Gwinner (2000), High Resolution Stereo Camera (HRSC)-Multipsectral 3D-data acquisition and photogrammetric data processing, *Can. J. Remote Sens.*, *26*(5), 466–474.

Williams, R. M. E., and R. J. Phillips (2001), Morphometric measurements of Martian Valley networks from Orbiter Laser Altimeter (MOLA) data, *J. Geophys. Res.*, *106*, 23,737–23,751, doi:10.1029/2000JE001409.

Wilson, S. A., and J. R. Zimbelman (2004), Latitude-dependent nature and physical characteristics of transverse aeolian ridges on Mars, *J. Geophys. Res.*, *109*, E10003, doi:10.1029/2004JE002247.

V. Ansan, E. Gailhardis, N. Mangold, and P. Masson, Laboratoire IDES-UMR 8148 CNRS, Bâtiment 509, Université Paris-Sud, F-91405 Orsay CEDEX, France. (veronique.ansan@u-psud.fr)

G. Neukum, Institute of Geosciences, FU Berlin, Malteserstrasse 74-100, D-12249 Berlin, Germany.